The Astrophysical Journal Letters, 983:L25 (19pp), 2025 April 10 https://doi.org/10.3847/2041-8213/adaeb7

The JWST Early Release Science Program for Direct Observations of Exoplanetary Systems. III. Aperture Masking Interferometric Observations of the Star HIP 65426 at 3.8 μm

Shrishmoy Ray[1,2], Steph Sallum[3], Sasha Hinkley[2], Anand Sivaramkrishnan[4], Rachel Cooper[4], Jens Kammerer[4], Alexandra Z. Greebaum[5], Deeparshi Thatte[4], Tomas Stolker[6], Cecilia Lazzoni[2], Andrei Tokovinin[7], Matthew de Furio[8], Samuel Factor[9], Michael Meyer[8], Jordan M. Stone[10], Aarynn Carter[11], Beth Biller[12,13], Andrew Skemer[11], Genaro Suárez[14], Jarron M. Leisenring[15], Marshall D. Perrin[4], Adam L. Kraus[9], Olivier Absil[16], William O. Balmer[4,17], Anthony Boccaletti[18], Mariangela Bonavita[19], Mickael Bonnefoy[20], Mark Booth[21], Brendan P. Bowler[9], Zackery W. Briesemeister[22], Marta L. Bryan[23], Per Calissendorff[8], Faustine Cantalloube[24], Gael Chauvin[25], Christine H. Chen[4,17], Elodie Choquet[24], Valentin Christiaens[16], Gabriele Cugno[8], Thayne Currie[26,27], Camilla Danielski[28], Trent J. Dupuy[29], Jacqueline K. Faherty[14], Michael P. Fitzgerald[30], Jonathan J. Fortney[11], Kyle Franson[9,81], Julien H. Girard[4], Carol A. Grady[31], Eileen C. Gonzales[32,82], Thomas Henning[33], Dean C. Hines[4], Kielan K. W. Hoch[34], Callie E. Hood[11], Alex R. Howe[22], Markus Janson[35], Paul Kalas[23,36,37], Grant M. Kennedy[38], Matthew A. Kenworthy[39], Pierre Kervella[18], Masayuki Kuzuhara[40], Anne-Marie Lagrange[18], Pierre-Olivier Lagage[41], Kellen Lawson[22], Ben W. P. Lew[42], Michael C. Liu[43], Pengyu Liu[44], Jorge Llop-Sayson[45], James P. Lloyd[32], Bruce Macintosh[46], Sebastian Marino[47,48], Mark S. Marley[49], Christian Marois[50], Raquel A. Martinez[51], Brenda C. Matthews[52], Elisabeth C. Matthews[53], Dimitri Mawet[45,54], Johan Mazoyer[18], Michael W. McElwain[22], Stanimir Metchev[55], Michael R. Meyer[8], Brittany E. Miles[11], Maxwell A. Millar-Blanchaer[56], Paul Molliere[33], Sarah E. Moran[49], Caroline V. Morley[9], Sagnick Mukherjee[11], Paulina Palma-Bifani[25], Eric Pantin[57], Polychronis Patapis[58], Simon Petrus[59,60], Laurent Pueyo[4], Sascha P. Quanz[58], Andreas Quirrenbach[61], Isabel Rebollido[4], Jea Adams Redai[62], Bin B. Ren[20], Emily Rickman[63], Matthias Samland[33], Joshua E. Schlieder[22], Glenn Schneider[15], Karl R. Stapelfeldt[54], Motohide Tamura[64], Xianyu Tan[65], Taichi Uyama[66], Arthur Vigan[24], Malavika Vasist[16], Johanna M. Vos[67,68], Kevin Wagner[15,83], Jason J. Wang[45,69], Kimberly Ward-Duong[70], Niall Whiteford[14], Schuyler G. Wolff[15], Kadin Worthen[17], Mark C. Wyatt[48], Marie Ygouf[54], Xi Zhang[11], Keming Zhang[23], Zhoujian Zhang[71], Yifan Zhou[9], Alice Zurlo[72,80], B. A. Sargent[4,73], Christopher A. Theissen[74], Elena Manjavacas[75], Anna Lueber[76], Daniel Kitzmann[77], Ben J. Sutlieff[12,78], and Sarah K. Betti[79]

[1] School of Mathematics and Physics, University of Queensland, St Lucia, QLD 4072, Australia
[2] University of Exeter, Astrophysics Group, Physics Building, Stocker Road, Exeter, EX4 4QL, UK
[3] Department of Physics and Astronomy, University of California, Irvine, 4129 Frederick Reines Hall, Irvine, CA 92697-4575, USA
[4] Space Telescope Science Institute, 3700 San Martin Drive, Baltimore, MD 21218, USA
[5] IPAC, Mail Code 100-22, Caltech, 1200 E. California Blvd., Pasadena, CA 91125, USA
[6] Leiden Observatory, Leiden University, Niels Bohrweg 2, 2333 CA Leiden, The Netherlands
[7] Cerro Tololo Inter-American Observatory, CTIO/AURA Inc., Casilla 603, La Serena, Chile
[8] Department of Astronomy, University of Michigan, 1085 S. University, Ann Arbor, MI 48109, USA
[9] Department of Astronomy, University of Texas at Austin, 2515 Speedway Stop C1400, Austin, TX 78712, USA
[10] Naval Research Laboratory, Remote Sensing Division, 4555 Overlook Ave SW, WA, DC 20375, USA
[11] Department of Astronomy & Astrophysics, University of California, Santa Cruz, 1156 High St, Santa Cruz, CA 95064, USA
[12] Scottish Universities Physics Alliance, Institute for Astronomy, University of Edinburgh, Blackford Hill, Edinburgh, EH9 3HJ, UK
[13] Centre for Exoplanet Science, University of Edinburgh, Edinburgh EH9 3HJ, UK
[14] Department of Astrophysics, American Museum of Natural History, Central Park West at 79th Street, NY 10024, USA
[15] Steward Observatory and the Department of Astronomy, The University of Arizona, 933 N Cherry Ave, Tucson, AZ 85721, USA
[16] Space sciences, Technologies & Astrophysics Research (STAR) Institute, Université de Liège, Allée du Six Août 19c, B-4000 Sart Tilman, Belgium
[17] Department of Physics & Astronomy, Johns Hopkins University, 3400 N. Charles Street, Baltimore, MD 21218, USA
[18] LESIA, Observatoire de Paris, Université PSL, CNRS, Université Paris Cité, Sorbonne Université, 5 place Jules Janssen, 92195 Meudon, France
[19] School of Physical Sciences, Faculty of Science, Technology, Engineering and Mathematics, The Open University, Walton Hall, Milton Keynes, MK7 6AA, UK
[20] Université Grenoble Alpes, Institut de Planétologie et d'Astrophysique (IPAG), F-38000 Grenoble, France
[21] Astrophysikalisches Institut und Universitätssternwarte, Friedrich-Schiller-Universität Jena, Schillergäßchen 2-3, D-07745 Jena, Germany
[22] NASA-Goddard Space Flight Center, 8800 Greenbelt Rd, Greenbelt, MD 20771, USA
[23] Department of Astronomy, 501 Campbell Hall, University of California Berkeley, Berkeley, CA 94720-3411, USA
[24] Aix Marseille Univ, CNRS, CNES, LAM, 13013 Marseille, France
[25] Laboratoire J.-L. Lagrange, Université Cote d'Azur, CNRS, Observatoire de la Cote d'Azur, 06304 Nice, France
[26] Department of Physics and Astronomy, University of Texas-San Antonio, 1 UTSA Circle, San Antonio, TX78249, USA
[27] Subaru Telescope,National Astronomical Observatory of Japan, 650 North A'ohōkū Place, Hilo, HI 96720, USA
[28] Instituto de Astrofísica de Andalucía, CSIC, Glorieta de la Astronomía s/n, 18008, Granada, Spain
[29] Institute for Astronomy, University of Edinburgh, Royal Observatory, Blackford Hill, Edinburgh, EH9 3HJ, UK
[30] University of California, Los Angeles, 430 Portola Plaza Box 951547, Los Angeles, CA 90095-1547, USA
[31] Eureka Scientific, 2452 Delmer. St., Suite 1, Oakland, CA 96402, USA
[32] Department of Astronomy and Carl Sagan Institute, Cornell University, 122 Sciences Drive, Ithaca, NY 14853, USA
[33] Max-Planck-Institut für Astronomie, Königstuhl 17, 69117 Heidelberg, Germany
[34] Center for Astrophysics and Space Sciences, University of California, San Diego, La Jolla, CA 92093, USA
[35] Department of Astronomy, Stockholm University, AlbaNova University Center, SE-10691 Stockholm, Sweden
[36] SETI Institute, Carl Sagan Center, 189 Bernardo Ave, Mountain View, CA 94043, USA

[37] Institute of Astrophysics, FORTH, GR-71110 Heraklion, Greece
[38] Department of Physics, University of Warwick, Gibbet Hill Road, Coventry, CV4 7AL, UK
[39] Leiden Observatory, Leiden University, P.O. Box 9513, 2300 RA Leiden, The Netherlands
[40] Astrobiology Center of NINS, 2-21-1, Osawa, Mitaka, Tokyo 181-8588, Japan
[41] Université Paris-Saclay, Université Paris Cité, CEA, CNRS, AIM, 91191, Gif-sur-Yvette, France
[42] Bay Area Environmental Research Institute and NASA Ames Research Center, Moffett Field, CA 94035, USA
[43] Institute for Astronomy, University of Hawai'i, 2680 Woodlawn Drive, Honolulu, HI 96822, USA
[44] Scottish Universities Physics Alliance, Institute for Astronomy, University of Edinburgh, Blackford Hill, Edinburgh, EH9 3HJ, UK; Centre for Exoplanet Science, University of Edinburgh, Edinburgh, EH9 3HJ, UK
[45] Department of Astronomy, California Institute of Technology, Pasadena, CA 91125, USA
[46] Kavli Institute for Particle Astrophysics and Cosmology, Stanford University, Stanford, CA 94305, USA
[47] Jesus College, University of Cambridge, Jesus Lane, Cambridge, CB5 8BL, UK
[48] Institute of Astronomy, University of Cambridge, Madingley Road, Cambridge, CB3 0HA, UK
[49] Dept. of Planetary Sciences, Lunar & Planetary Laboratory, University of Arizona, Tucson, AZ 85721, USA
[50] National Research Council of Canada, Canada
[51] Department of Physics and Astronomy, 4129 Frederick Reines Hall, University of California, Irvine, CA 92697, USA
[52] Herzberg Astronomy & Astrophysics Research Centre, National Research Council of Canada, 5071 West Saanich Road, Victoria, BC V9E 2E7, Canada
[53] Observatoire de l'Université de Genève, Chemin Pegasi 51, 1290 Versoix, Switzerland
[54] Jet Propulsion Laboratory, California Institute of Technology, 4800 Oak Grove Drive, Pasadena, CA 91109, USA
[55] Western University, Department of Physics & Astronomy and Institute for Earth and Space Exploration, 1151 Richmond Street, London, Ontario, N6A 3K7, Canada
[56] Department of Physics, University of California, Santa Barbara, CA 93106, USA
[57] IRFU/DAp Département D'Astrophysique CE Saclay, Gif-sur-Yvette, France
[58] Institute of Particle Physics and Astrophysics, ETH Zurich, Wolfgang-Pauli-Str. 27, 8093 Zurich, Switzerland
[59] Instituto de Física y Astronomía, Facultad de Ciencias, Universidad de Valparaíso, Av. Gran Bretaña 1111, Valparaíso, Chile
[60] Núcleo Milenio Formacíon Planetaria—NPF, Universidad de Valparaíso, Av. Gran Bretaña 1111, Valparaíso, Chile
[61] Landessternwarte,Zentrum für Astronomie der Universität Heidelberg, Königstuhl 12, D-69117 Heidelberg, Germany
[62] Center for Astrophysics | Harvard & Smithsonian, 60 Garden Street, Cambridge, MA 02138, USA
[63] European Space Agency (ESA), ESA Office, Space Telescope Science Institute, 3700 San Martin Drive, Baltimore, MD 21218, USA
[64] The University of Tokyo, 7-3-1 Hongo, Bunkyo-ku, Tokyo 113-0033, Japan
[65] Tsung-Dao Lee Institute, Shanghai Jiao Tong University, 520 Shengrong Road, Shanghai, People's Republic of China
[66] IPAC, California Institute of Technology, 1200 E. California Blvd., Pasadena, CA 91125, USA
[67] School of Physics, Trinity College Dublin, The University of Dublin, Dublin 2, Ireland
[68] Department of Astrophysics, American Museum of Natural History, New York, NY 10024, USA
[69] Center for Interdisciplinary Exploration and Research in Astrophysics (CIERA) and Department of Physics and Astronomy, Northwestern University, Evanston, IL 60208, USA
[70] Department of Astronomy, Smith College, Northampton, MA 01063, USA
[71] Department of Astronomy & Astrophysics, University of California, Santa Cruz, CA 95064, USA
[72] Instituto de Estudios Astrofísicos, Facultad de Ingeniería y Ciencias,Universidad Diego Portales, Av. Ejército Libertador 441, Santiago, Chile
[73] Center for Astrophysical Sciences, The William H. Miller III Department of Physics and Astronomy, Johns Hopkins University, Baltimore, MD 21218, USA
[74] Department of Astronomy & Astrophysics, University of California, San Diego, La Jolla, CA 92093, USA
[75] AURA for the European Space Agency (ESA), ESA Office, Space Telescope Science Institute, 3700 San Martin Drive, Baltimore, MD 21218, USA
[76] Ludwig Maximilian University, University Observatory Munich, Scheinerstrasse 1, Munich D-81679, Germany
[77] Center for Space and Habitability, University of Bern, Gesellschaftsstrasse. 6, 3012 Bern, Switzerland
[78] Centre for Exoplanet Science, University of Edinburgh, Edinburgh, EH9 3HJ, UK
[79] Space Telescope Science Institute (STScI), 3700 San Martin Drive, Baltimore, MD 21218, USA
Received 2023 October 17; revised 2024 December 22; accepted 2025 January 19; published 2025 April 9

Abstract

We present aperture masking interferometry (AMI) observations of the star HIP 65426 at 3.8 μm, as part of the JWST Direct Imaging Early Release Science program, obtained using the Near Infrared Imager and Slitless Spectrograph instrument. This mode provides access to very small inner working angles (even separations slightly below the Michelson limit of $0.5\lambda/D$ for an interferometer), which are inaccessible with the classical inner working angles of the JWST coronagraphs. When combined with JWST's unprecedented infrared sensitivity, this mode has the potential to probe a new portion of parameter space across a wide array of astronomical observations. Using this mode, we are able to achieve a 5σ contrast of $\Delta m_{\rm F380M} \sim 7.62 \pm 0.13$ mag relative to the host star at separations $\gtrsim 0\farcs07$, and the contrast deteriorates steeply at separations $\lesssim 0\farcs07$. However, we detect no additional companions interior to the known companion HIP 65426b (at separation $\sim 0\farcs82$ or 87^{+108}_{-31} au). Our observations thus rule out companions more massive than 10–12 $M_{\rm Jup}$ at separations ~10–20 au from HIP 65426, a region out of reach of ground- or space-based coronagraphic imaging. These observations confirm that the AMI mode on JWST is sensitive to planetary mass companions at close-in separations ($\gtrsim 0\farcs07$), even for thousands of more distant stars

[80] Millennium Nucleus on Young Exoplanets and their Moons (YEMS).
[81] NSF Graduate Research Fellow.
[82] 51 Pegasi b Fellow.
[83] NASA Hubble Fellowship Program—Sagan Fellow.

at ∼100 pc, in addition to the stars in the nearby young moving groups and associations, as stated in previous works. This result will allow the planning and successful execution of future observations to probe the inner regions of nearby stellar systems, opening an essentially unexplored parameter space.

Unified Astronomy Thesaurus concepts: High contrast techniques (2369); Exoplanet astronomy (486); James Webb Space Telescope (2291); Direct detection interferometry (386)

1. Introduction

JWST (J. P. Gardner et al. 2006, 2023) has established itself as the world's pre-eminent infrared observatory. The Near-Infrared Imager and Slitless Spectrograph instrument (NIRISS; R. Doyon et al. 2012, 2023) is equipped with a sparse aperture mask (A. Sivaramakrishnan et al. 2009, 2023). This mask enables the Aperture Masking Interferometry (AMI; J. E. Baldwin et al. 1986; C. A. Haniff et al. 1987; A. C. S. Readhead et al. 1988) mode on the telescope, which is available for the first time from space. This facilitates the execution of science cases that can use moderate contrast at small angular separations—for example, high-resolution imaging of extended sources, structure identification of solar system objects (e.g., Jupiter's moon Io), and imaging extremely bright objects like Wolf–Rayet stars (R. M. Lau et al. 2024).

A particularly powerful feature of this mode is its ability to directly image planetary mass companions (PMCs) inside the Rayleigh diffraction limit, $\lesssim\lambda/D$ (where D is the aperture size of the telescope and λ is the observing wavelength). With the JWST/NIRISS/AMI mode, contrasts of $\sim10^{-3}$–10^{-4} are predicted to be achievable with sufficient integration times (A. Soulain et al. 2020; J. Rigby et al. 2023). This mode is well equipped to directly detect or place constraints on additional inner companions of systems with already known wide-separation companions. Such systems have historically revealed the presence of additional companions at smaller orbital separations (C. Marois et al. 2010; M. Nowak et al. 2020; S. Hinkley et al. 2023), which has also been demonstrated by theoretical studies (K. Wagner et al. 2019). Using AMI to expand the parameter space inward will hence enable the community to provide a more robust characterization of the orbital architectures of planetary systems. In addition to this, the mode is also predicted to access Jupiter-mass companions at water–frost-line separations around stars in nearby young moving groups and associations (S. Sallum et al. 2019; S. Ray et al. 2023). Going forward, this will be a promising technique for placing constraints on initial entropies (by using in conjunction planetary mass estimates, from Gaia or long-term orbital monitoring) of planets for at least the next decade (D. S. Spiegel & A. Burrows 2012; S. Ray et al. 2023).

The Director's Discretionary Early Release Science (DD-ERS) Program 1386 (S. Hinkley et al. 2022) includes AMI observations to demonstrate the observing mode and test its feasibility for these science cases. In this Letter, we report the results of the AMI observations of the ERS program, of the star HIP 65426 (A2V, 109.20 ± 0.74 pc), observed at 3.8 μm. This star has a previously known companion, HIP 65426b (G. Chauvin et al. 2017; A. C. Cheetham et al. 2019), with a projected separation of 86^{+116}_{-31} au and a mass of 7.1 ± 1.2 $M_{\rm Jup}$ (A. L. Carter et al. 2023). In this Letter, we present the scientific results of the ERS 1386 AMI observations, placing new constraints on the presence of additional companions in the HIP 65426 system and demonstrating its potential for similar observations in other nearby systems. In an accompanying Letter (S. Sallum et al. 2024), we analyze the performance, achievable contrast, and limiting noise sources of this mode.

This work was carried out in parallel with other science aspects of the ERS program. These included: (1) coronagraphic observations of HIP 65426b at 2–5 μm with the Near-Infrared Camera and 11–16 μm with the Mid-Infrared Instrument (A. L. Carter et al. 2023); (2) the highest-fidelity spectrum to date of a planetary mass object, VHS 1256b (B. E. Miles et al. 2023); and (3) coronagraphy out to 15.5 μm of HD 141569A, a young circumstellar disk, with a particular focus on sampling the disk brightness on and off the 3.0 μm H_2O ice feature (E. Choquet et al. 2025, in preparation; M. Millar-Blanchaer et al. 2025, in preparation).

In Section 2, we give a brief summary of the AMI mode with JWST, followed by our observation strategy in Section 3. In Section 4, we detail the various data processing steps. In Section 5, we summarize our discussion, and in Section 6, we present the principal conclusions of this study.

2. JWST AMI

AMI transforms a conventional telescope into an interferometric array via a pupil-plane mask (P. G. Tuthill et al. 2001). This is typically accomplished using a piece of metal with holes (subapertures) cut out of it. The images recorded by the detector are then the interference fringes produced from the light after passing through the subapertures, which can be analyzed using Fourier techniques. When each baseline in an aperture mask has a unique position angle and separation, a linear relationship between pupil-plane phase differences and the measured fringe phase exists. Due to this nonredundancy, Fourier observables (e.g., closure phases and squared visibilities; see Section 4.2) can be calculated that are robust to first-order residual phase errors (following the description in M. J. Ireland 2013).

This technique has been successfully carried out using ground-based facilities (e.g., P. G. Tuthill et al. 2000; J. D. Monnier et al. 2007; A. L. Kraus & M. J. Ireland 2012; S. Hinkley et al. 2015) and is for the first time being executed in space with JWST (J. Kammerer et al. 2023; A. Sivaramakrishnan et al. 2023). This is achieved using a mask with seven hexagonal subapertures (see Figure 1), each of which has an in-circle diameter of 0.8 m, when projected onto the JWST primary mirror (A. Sivaramakrishnan et al. 2012; A. Z. Greenbaum et al. 2015). This probes $\binom{7}{2}$ or 21 distinct spatial frequencies (number of baselines) and $\binom{7}{3}$ or 35 closure-phase triangles.[84] This mode can be used with four NIRISS filters at wavelengths 2.77 μm (F277W), 3.80 μm (F380M), 4.30 μm (F430M), and 4.80 μm (F480M). These wavelength channels are specifically designed to be sensitive to H_2O,

[84] For a set with n elements, the number of combinations with k groups is $\binom{n}{k}=\frac{n!}{k!(n-k)!}$. Since the mask has seven subapertures, $n=7$, and $k=2$ for baselines (two endpoints of a line segment) and $k=3$ for closure phases (three vertices of a triangle).

Table 1
Parameters for the NIRISS/AMI Observations in the F380M Filter

Star	Type	Start Time	End Time	Sequence	Readout	N_{groups}	N_{ints}	Dithers	t_{exp} (s)
HD 115842	Calibrator	05:26:46	06:52:10	1a	NISRAPID	2	10,000	1	2468.00
				1b	NISRAPID	2	5500	1	1357.40
HIP 65426	Target	07:02:39	10:53:00	2a	NISRAPID	13	10,000	1	10,766.40
				2b	NISRAPID	13	950	1	1022.81
HD 116084	Calibrator	11:02:17	12:49:58	3a	NISRAPID	3	10,000	1	3222.4
				3b	NISRAPID	3	6000	1	1933.44

Note. The observations were executed on 2022 July 30 (UTC). The start and the end times indicate the start and the end of the observation block at UTC and are not directly related to the exposure times. The target star HIP 65426 was observed between the calibrator stars HD 115842 and HD 116084.

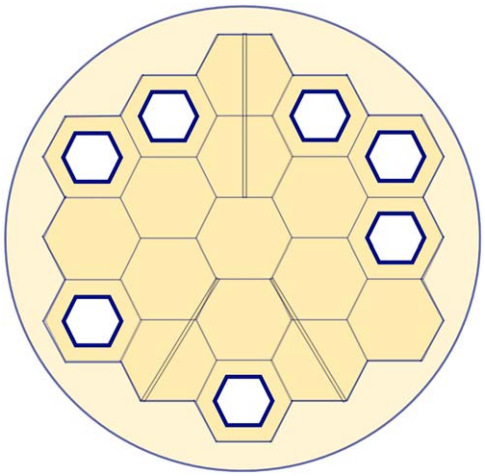

Figure 1. Schematic diagram of the nonredundant mask on board JWST/NIRISS containing seven subapertures.

CH_4, CO_2, and CO features, respectively (e.g., Figure 1 of A. Soulain et al. 2020).

3. Observing Strategy

The AMI observations were performed using the F380M filter and the SUB80 subarray with the NISRAPID readout pattern and no dithering. The F380M filter was specifically chosen from the available filters to reach smaller angular separations than the F430M and F480M filters, to detect close-in companions while making sure the central wavelength was close to the region of the spectrum where exoplanets are the brightest (at ∼4–5 μm; e.g., Figure 2 of S. Ray et al. 2023—as compared to the F277W filter, which typically spans wavelengths where directly imaged exoplanets are relatively faint).

The observing setup was designed such that a photon-noise-limited observation would be able to access a contrast of $\Delta_{mag} \sim 10$ (M. J. Ireland 2013). The appropriate numbers of groups and integrations were hence chosen to collect $\sim 10^{10}$ photons for each target while avoiding saturation or nonlinearity effects, as presented in Table 1 (see Appendix A for an explanation of the terms "groups" and "integrations"). Table 1 also presents the UTC start and end times of the observations of the target and calibrator stars. And t_{exp} is the total exposure time for each observation sequence. All the observations were carried out following the recommended best practices as known prior to launch and described in the JWST user documentation.[85]

To ensure optimal data analysis of the AMI observations, point-spread-function (PSF) reference stars are required to be observed, in addition to the science target. This is executed because even though Fourier observables are robust to phase errors to first order, higher-order errors remain that must be calibrated out (M. J. Ireland 2013). These reference stars should be point sources, so that they measure only the instrumental contributions to the errors in the observables, which, in turn, ensures the optimal calibration of the target star observations. The target star was planned to be observed with the most time and the calibrators were chosen to be relatively bright stars, close to the target star on the sky plane. This ensured that we obtained similar numbers of photons from the calibrators as the target star, with shorter exposure times (see Table 1). Each calibrator had a total exposure time of ∼1 hr and the target star had an exposure time of ∼3 hr. However, for future observations with this mode, calibrators with similar brightness as the target star should be chosen, as the detector systematics are the limiting factor in terms of reaching the required contrast for data sets of this depth (see Section 4.2 and S. Sallum et al. 2024 for more details).

For the AMI sequence of this program, the observation of the target star HIP 65426 was preceded by one calibrator (HD 115842) and followed by another calibrator (HD 116084; see Section 3.1 for details). Observations of two calibrator stars reduce the risk of encountering calibrators with unexpected resolved structure (e.g., close-in companions and disks). Observing the target star in the middle of the sequence between two calibrator stars that are close on the sky plane (1) is advantageous toward reducing the wave-front drift, and (2) ensures that the time elapsed during the slew between the target and the reference stars is kept to a minimum, which minimizes thermal drift due to pointing changes. This ensures that the changing spacecraft altitude does not cause a change in the temperature of the primary mirror segments and subsequently affect the Fourier phases observed by the telescope. The PSF reference stars are then used to calibrate out instrumental contributions to the interferometric observables (see Section 4). A raw image taken with the JWST/NIRISS/AMI mode of the science target (HIP 65426) is shown in the left panel of Figure 2.

[85] https://jwst-docs.stsci.edu/jwst-near-infrared-imager-and-slitless-spectrograph/niriss-observing-strategies/niriss-ami-recommended-strategies

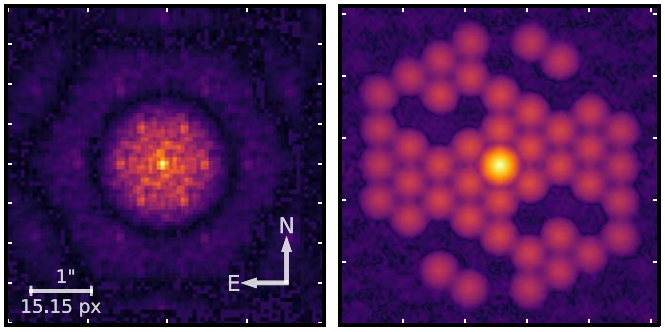

Figure 2. On the left is the science raw image of HIP 65426. This pattern (interferogram) is obtained on the detector and is a result of the interference of the light emerging from each of the subapertures of the mask, as shown in Figure 1. On the right is the associated power spectrum of the science image, which is the modulus squared of its Fourier transform. The power spectrum is used to extract the orbital properties of a potential companion in the star system by analyzing the Fourier observables. The observations in the figure are taken at 3.80 μm.

Table 2
SOAR Observations of the JWST Calibrators at Separations $\theta_1 = 0\farcs15$ and $\theta_2 = 1\farcs00$

Calibrator	Filter	Δm_{θ_1}	Δm_{θ_2}
HD 115842	I (0.8 μm)	2.71	5.00
	y (0.5 μm)	3.66	5.47
HD 116084	I (0.8 μm)	2.97	5.10
	y (0.5 μm)	3.44	5.45

Note. The quantities Δm_{θ_1} and Δm_{θ_2} are the achieved contrasts at the separations θ_1 and θ_2, respectively. These stars were observed prior to the JWST observations, to check them for any potential companions or extended sources.

3.1. Vetting of the Calibrator Stars

To ensure the calibrator stars—HD 115842 and HD 116084—were point sources, they were vetted first using `SearchCal` (D. Bonneau et al. 2006) and were then followed up with observations using ground-based facilities. This was first done with the speckle imaging observations from Southern Astrophysical Research (SOAR) telescope's High Resolution Camera (A. Tokovinin et al. 2010) instrument. Both calibrators (HD 115842 and HD 116084) were found to be unresolved point sources. This result is presented in Table 2. For the calibrator HD 115842, the limiting contrasts at $0\farcs15$ and $1\farcs00$ were found to be $\Delta m \sim 2.71$ and $\Delta m \sim 5.00$ respectively at 0.8 μm, and $\Delta m \sim 3.66$ and $\Delta m \sim 5.47$ respectively at 0.5 μm. And for the calibrator HD 116084, the limiting contrasts at $0\farcs15$ and $1\farcs00$ were found to be $\Delta m \sim 2.97$ and $\Delta m \sim 5.10$ respectively at 0.8 μm, and $\Delta m \sim 3.44$ and $\Delta m \sim 5.45$ respectively at 0.5 μm.

To check the reference stars further with higher sensitivity, we also observed them with AMI observations using the Very Large Telescope (VLT)/SPHERE/integral field spectrograph (IFS; A. C. Cheetham et al. 2016; Proposal ID: 109.24EY). Both stars were found to be unresolved point sources, with an average contrast limit of $\Delta_{\rm mag} \sim 6$, calculated across the 39 IFS wavelength bins. There were no significant variations on the limit of the contrast as a function of position angle. This contrast was achieved at separations of $\sim\lambda/D$ for both stars, which corresponds to separations of 23–40 mas given the IFS wavelength range of 0.95–1.60 μm.

4. Data Reduction and Extraction of Fourier Observables

As part of the science-enabling products produced by this ERS team, we have developed `SAMpy`[86] (S. Sallum et al. 2022), which primarily handled the processing of this data set, in conjunction with the `jwst`[87] (H. Bushouse et al. 2022) pipeline.[88] `SAMpy` is a publicly available PYTHON package, containing data reduction tools tailored for JWST/NIRISS/AMI, and is flexible enough to adapt to arbitrary masking setups (e.g., VLT/SPHERE, Large Binocular Telescope/LMIRCam, and Keck/NIRC2). It processes the AMI data using a Fourier-plane approach. The accompanying Letter by S. Sallum et al. (2024) presents a detailed description and justification of the processing steps undertaken for this data set, which is briefly outlined in the following sections for clarity.

4.1. Preprocessing of the Data

To prepare the data for the calculation of the Fourier observables, some preprocessing steps using `SAMpy` were executed. The first step in this process was to identify and correct bad pixels. First, the bad-pixel map was produced by the `jwst` stage 1 pipeline, which flags all "DO NOT USE" pixels in the data quality array as bad. This was followed by identifying additional bad pixels using the statistics of the individual integrations and the set of integrations. All such bad pixels were corrected, using the Fourier-plane approach taken in J. Kammerer et al. (2019). Finally, each image was centered to pixel-level precision, cropping to a smaller size of 64×64 pixels, before applying a fourth-order super-Gaussian window with an FWHM of 48 pixels. This process is described in detail in S. Sallum et al. (2024).

4.2. Data Processing and Model Fitting

Once the processed image was obtained, the Fourier observables were calculated from the Fourier transform of the image (the power spectrum is shown in the right panel of Figure 2). First, the complex visibilities were calculated, which comprise the amplitudes and phases associated with the unique mask baselines. This was followed by the calculation of squared visibilities, which are the powers (amplitudes squared) associated with each of the unique mask baselines. Next, the closure phases were computed, which are the sums of phases for baselines forming a triangle.

After the calculation of the above, the observations were calibrated. Calibrating the observations for the science target (HIP 65426) was explored by calibrating it separately with each of the calibrator stars, HD 115842 and HD 116084, respectively, in addition to calibrating it with both the calibrator stars together. It was found that using HD 116084 solely to calibrate the science target yielded the best results in terms of reaching the deepest contrast ($\Delta m_{\rm F380M} \sim 7.8$; see the third column of the top panel of Figure 3). The two likely reasons for this are that this observation (1) had more similar charge migration properties to HIP 65426 (see Section 5.1), and (2) used a larger number of groups (three, as opposed to two for HD 115852).

[86] https://github.com/JWST-ERS1386-AMI/SAMpy
[87] https://jwst-pipeline.readthedocs.io
[88] All data were processed using pipeline version `jwst` = 1.7.1.

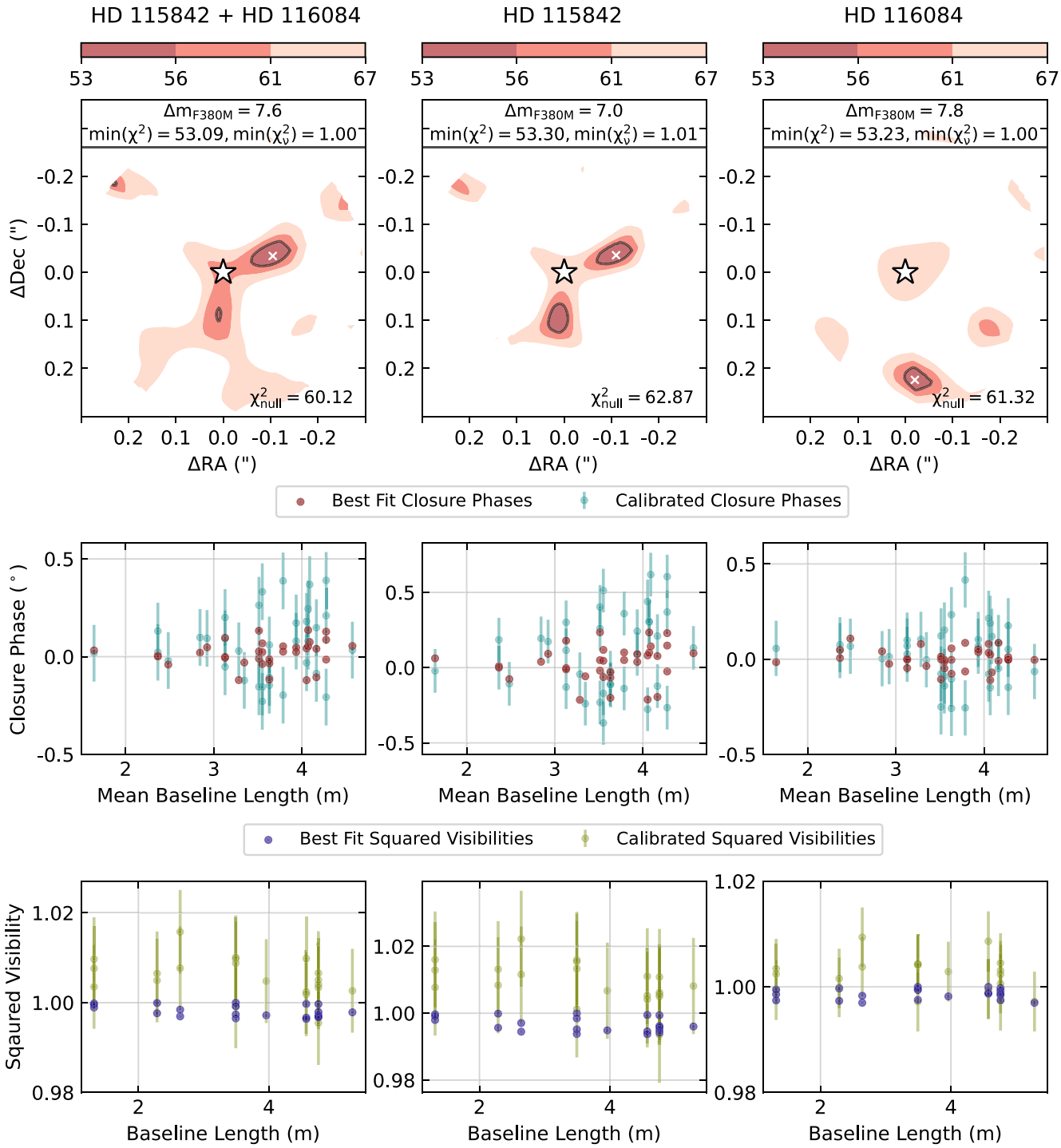

Figure 3. The first column shows the HIP 65426 data calibrated with both calibrators (HD 115842 and HD 116084), the second column shows the data calibrated with only HD 115842, and the third column shows the data calibrated with only HD 116084. The first row shows the χ^2 surfaces that are slices of the best-fit contrast containing the lowest χ^2 from a grid search (with parameters of companion separation, position angle, and contrast) in R.A. and decl. This is shown for each HIP 65426 calibration. The second and third rows show the corresponding best-fit Fourier observables of closure phases and squared visibilities, respectively, compared to the data. The "⋆" symbols in the χ^2 maps in the first row show the position of the central star, and the "×" symbols show the best-fit companion positions for each calibration. The best-fit Δm_{F380M} contrast value for each calibration is also displayed in the panels of the first row. Along with this, the minimum χ^2 values and the minimum reduced χ^2 values (denoted by χ^2_ν) are also displayed. Contour regions show the 1σ, 2σ, and 3σ regions respectively from the lowest χ^2 value. The 1σ regions are demarcated with a black contour for clarity. As discussed in Section 4.3, we conclude that no companions are detected, based on: (1) the inconsistent companion solutions from calibration to calibration; (2) the lack of a single clearly defined region of a low χ^2 value for individual calibrations; and (3) the similarity of these fit result values to those for simulated noise (see Figure 4).

Both of these characteristics result in better minimization of the PSF artifacts and detector systematics during data reduction and subsequent AMI calibration, making for a better-calibrated data set (S. Sallum et al. 2024). Hence, only HD 116084 was used for the calibration and the subsequent analysis in this Letter.

The calibration was done by: (1) dividing the squared visibilities of the target by those of the calibrator; and (2)

Table 3
This Table Shows the Best-fit Parameters (Equivalently, the Values Corresponding to the Lowest χ^2 Positions on the χ^2 Maps) from the Grid Search of the Reduced Data for Different Calibrations

	HD 115842 + HD 116084	HD 115842	HD 116084
Position Angle (deg)	$288.00^{+10.29}_{-10.28}$	$288.00^{+10.29}_{-2.02}$	$185.14^{+5.88}_{-1.54}$
Contrast (Δm_{F430M})	$7.6^{+1.4}_{-0.8}$	$7.0^{+1.0}_{-0.6}$	$7.8^{+1.0}_{-0.2}$
Separation (arcsec)	$0.11^{+0.04}_{-0.49}$	$0.12^{+0.03}_{-0.06}$	$0.23^{+0.02}_{-0.03}$

Note. The corresponding error for each value is the 1σ error from the best fit as shown in Figure 3.

subtracting the closure phases of the calibrator from the target closure phases (see Figure 3). As described in S. Sallum et al. (2024), we calculate both statistical error bars and systematic error bars for the closure phases and squared visibilities. We calculate statistical error bars by measuring the standard deviation of each quantity across all calibrated integrations. However, these are significantly smaller than the residual calibration errors in the data. We thus also estimate the systematic error bars by measuring the standard deviations of the closure phases and squared visibilities across the triangles and baselines, respectively. All the stars (namely, the target HIP 65426 and the calibrators HD 115842 and HD 116084) were found to have no systematic variation of visibility with baseline length and hence were unresolved.

As described in more detail in the accompanying Letter (S. Sallum et al. 2024), the closure-phase scatter can have contributions from random (for example, Poisson) noise and systematic noise. As an example of connecting the standard deviations of closure phases across triangles to noise sources, we can first consider the case where Poisson noise dominates. Each closure phase would have an error bar determined by the standard error (i.e., the standard deviation of the closure phase as measured across N frames, divided by the square root of the number of frames, N). This means that the distribution of the closure phases across the different triangles would have a standard deviation equal to that same standard error (assuming that each triangle has the same standard error).

We measure the standard deviations of the closure phases across the different triangles under the assumption that the systematic errors are approximately equal for all closing triangles, and that they are (similar to the Poisson noise description above) well modeled by a Gaussian distribution. In reality, different closing triangles might have different levels of both random and systematic errors. This is because the levels of Poisson noise vary with raw visibility amplitude, and systematic errors (which have many sources) are unlikely to be uniform with spatial frequency. However, the systematic errors cannot be measured more robustly than this, given the available data.

To test whether the scatter in the calibrated data (for HIP 65426 as well as for the two calibrators calibrated against one another) can be well modeled by a Gaussian distribution, we compare the closure phases across triangles to many realizations of random closure phases drawn from a Gaussian distribution with the same standard deviation. This procedure reproduces the data reliably. We thus determine these statistical errors to be adequate, given the limitations in our ability to measure systematic errors.

This method of estimating error bars is conservative, since the scatter in the closure phases across triangles is affected by both signal and noise. We thus only adopt these error bars after determining that the best fit (corresponding to the lowest χ^2 value) to the data set is indeed caused by noise. We do this first by examining the quality of the best fit, by calculating its reduced χ^2 value if only the standard errors were used, which for the fit to the HIP 65426 data calibrated with HD 116084 was calculated to be $\sim$41. This high reduced χ^2 value implies that the errors are indeed underestimated. Hence, larger errors on closure phases ($\sim 0\overset{\circ}{.}14$) were adopted by calculating the standard deviation, as previously mentioned, across all the measured closure phases for this calibration. This produced a reduced χ^2 of $\sim$1 for the best fit (see Figure 3). These adopted errors were used for all our analyses in this work.

4.3. Companion Model Fitting and Injection Tests

We fit companion models to the calibrated Fourier observables on the calibrated data set via both grid and Markov Chain Monte Carlo (MCMC) methods (utilizing the `emcee` PYTHON package; D. Foreman-Mackey et al. 2013). The analytic models consist of a delta function central point source (representing the star) and an ensemble of delta function companions each with a separation, position angle, and contrast relative to the central star, individually selected with the aim of obtaining a binary model (containing the central star and one companion) most closely resembling the calculated Fourier observables. This was achieved by varying the values of separation, position angle, and contrast of the companion delta function. We then take the lowest χ^2 value as the best-fit companion model. This χ^2 value of the best fit should be significant[89] compared to the null model for a confident detection.

To visualize this, we plot the χ^2 surface at the best-fit contrast slice (the one with the lowest χ^2 value) from the grid for each calibration in Figure 3. We also plot the 1σ, 2σ, and 3σ contour regions from the lowest χ^2 value. Since the companion model has three parameters, these are at values greater by 3.53, 8.02, and 14.16 respectively than the lowest χ^2 value. We also state the reduced minimum χ^2 values (denoted by χ^2_ν) in the figure.[90] The typical values of the minimum χ^2 and the null χ^2 for the calibrated data were calculated to be $\sim$53 and $\sim$61 (see the top panel of Figure 3), respectively. Hence, the best fits in each calibration are at values $<3\sigma$ from the null model, which is a statistically insignificant companion signal. The results of this reduction for each calibration are summarized in Table 3.

[89] For the purposes of this work, we state values at $\geqslant 5\sigma$ from the null value to be statistically significant.

[90] $\chi^2_\nu = \frac{\chi^2}{\kappa}$, where $\kappa = 53$, the number of degrees of freedom. This is calculated as $\kappa = 35+21-3$, where the first, second, and third terms are the number of closure phases, the number of squared visibilities, and the number of parameters (namely, the position angle, separation, and contrast) used in the grid search, respectively.

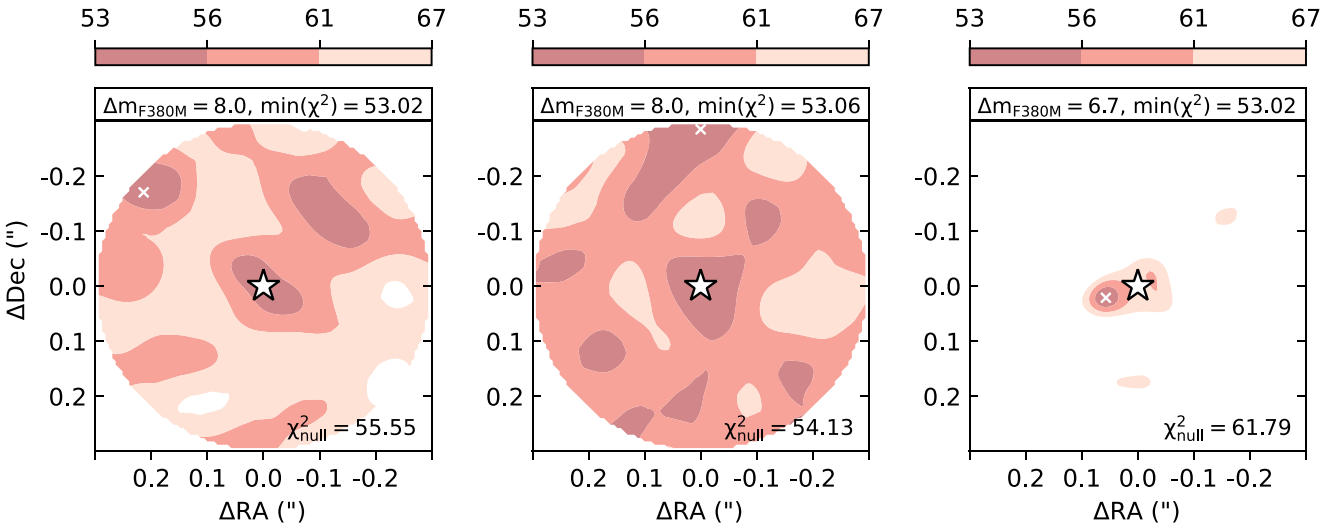

Figure 4. These plots show the χ^2 maps for three Gaussian distribution simulations, with the same mean and standard deviation as measured for the data set HIP 65426 calibrated with HD 116084. The contour regions show the 1σ, 2σ, and 3σ regions respectively from the lowest χ^2 value, similar to Figure 3. At the tops of these plots are the best-fit Δm_{F380M} contrast value along with the minimum value of χ^2 on the map. This minimum χ^2 location in the above plots is denoted by "×." These contrast values approximately overlap with the best-fit contrasts for the HIP 65426 companion fit, and the χ^2 surfaces display the same lack of a single, clearly defined low minimum. Together, these factors demonstrate that the fit results for HIP 65426 can be caused by noise alone. This further demonstrates that the statistically insignificant companion signals detected in Figure 3 are likely noise artifacts in the data rather than indicating the existence of an actual companion.

The best-fit (lowest-χ^2) values are presented with the 1σ error bars for each parameter.

While a best-fit model can be found for each data set, the best-fit models differ from one calibration to another, with contrasts between $\Delta m_{F380M} = 7.0$–7.8 and widely varying separations and position angles. Furthermore, in all three calibrations, a unique, clearly defined region of low-χ^2 values does not exist. It should be noted that the method for estimating systematic error bars (measuring the standard deviation of the time-averaged closure phases and squared visibilities) causes the reduced χ^2 values of the best fits in Figure 3 to be close to 1. This does not necessarily represent the quality of the fit but rather the large systematic uncertainties in the calibrated data. Thus, the inconsistent solutions from calibration to calibration, the lack of a clearly defined single χ^2 minimum, and the best-fit values being statistically insignificant ($<3\sigma$) when compared to the null model in any individual calibration argue against the existence of additional companions in this data set.

We used noise and companion injection simulations to explore this further, specifically for the HD 116084 calibration, since it yielded the lowest scatter and thus the deepest achievable contrast. We first performed fits to simulated Gaussian distributions. These were the closure phases and squared visibilities drawn from Gaussian distributions with standard deviations equal to those measured in the calibrated data. The mean of the closure-phase distribution was set equal to zero, and the mean of the squared visibility distribution was set to be the median value of the calibrated squared visibilities.

Figure 4 shows the resulting χ^2 maps at the best-fit companion contrast for three different realizations. The best-fit contrasts, which range from $\Delta m_{F380M} = 6.7$–8.0, overlap with the $\Delta m_{F380M} = 7.8$ mag result for HIP 65426. The typical value of the minimum χ^2 (best fit) in these is ∼53 and the null model values are ∼54–61. The best fits are hence at values $<3\sigma$ from the null model for all realizations, similar to the best fits of the calibrated data. This shows that the companion fit result shown in the right column of Figure 3 can be caused by noise alone. Specifically, companion contrasts of $\Delta m_{F380M} = 8.0$ are unreliable at wide separations (as seen in the left and center panels of Figure 4), and $\Delta m_{F380M} = 6.7$ at separations well within λ/D (∼at $0.5\lambda/D$, as seen in the right panel of Figure 4). The unreliability arises from the fact that there is no statistically significant unique low-χ^2 region. These fits to Gaussian distributions are consistent with the calculated contrast curve in Section 4.4 (also see Figures 5 and 6), since they are all below the curve, given their separations.

For clarity, in Figure 5, we show χ^2 maps of the calibrated (with HD 116084) data (HIP 65426) with injected companions. This was done by using a companion model constructed with given values of separation, contrast, and position angle. The Fourier observables (closure phases and squared visibilities) of this model were injected into the calibrated Fourier observables (closure phases and squared visibilities) of the data. This was achieved by adding the closure phases and multiplying the squared visibilities of the model and the data. The resulting closure phases and squared visibilities are presented in Appendix B and Appendix C, respectively. The errors for this were set to be the same as the errors of the calibrated data. Companions were injected at a position angle of $\theta = 60°$ (calculated counterclockwise with respect to the vertical axis), with varying contrasts and separations for six tests. Subsequently, a recovery was performed, following the same approach as for the real data. In Figure 5, the detection significance σ is given by k (analogous to the $\Delta\chi^2$ value discussed later in Section 4.4, $k = \mathrm{int}(\sqrt{\Delta\chi^2}) = \mathrm{int}(\sqrt{\chi^2_{null} - \chi^2_{min}})$) for each injection test. For tests with values of $k > 3\sigma$, the contour regions plotted are at $k\sigma$, $(k-1)\sigma$, and $(k-2)\sigma$ from the null (no-companion) χ^2 value.

The injected companions with $m_{F380M} \lesssim 7.5$ (the contrast limit from the 5σ contrast curve discussed in Section 4.4, shown in Figure 6) at separations beyond the Michelson diffraction limit ($0.5\lambda/D$) are clearly detected as distinct regions of low-χ^2 values (with $k \geqslant 5\sigma$), with preferred positions (in tests 3, 4, 5, and 6) in the first two rows of Figure 5, unlike the noise realizations and the calibrated data

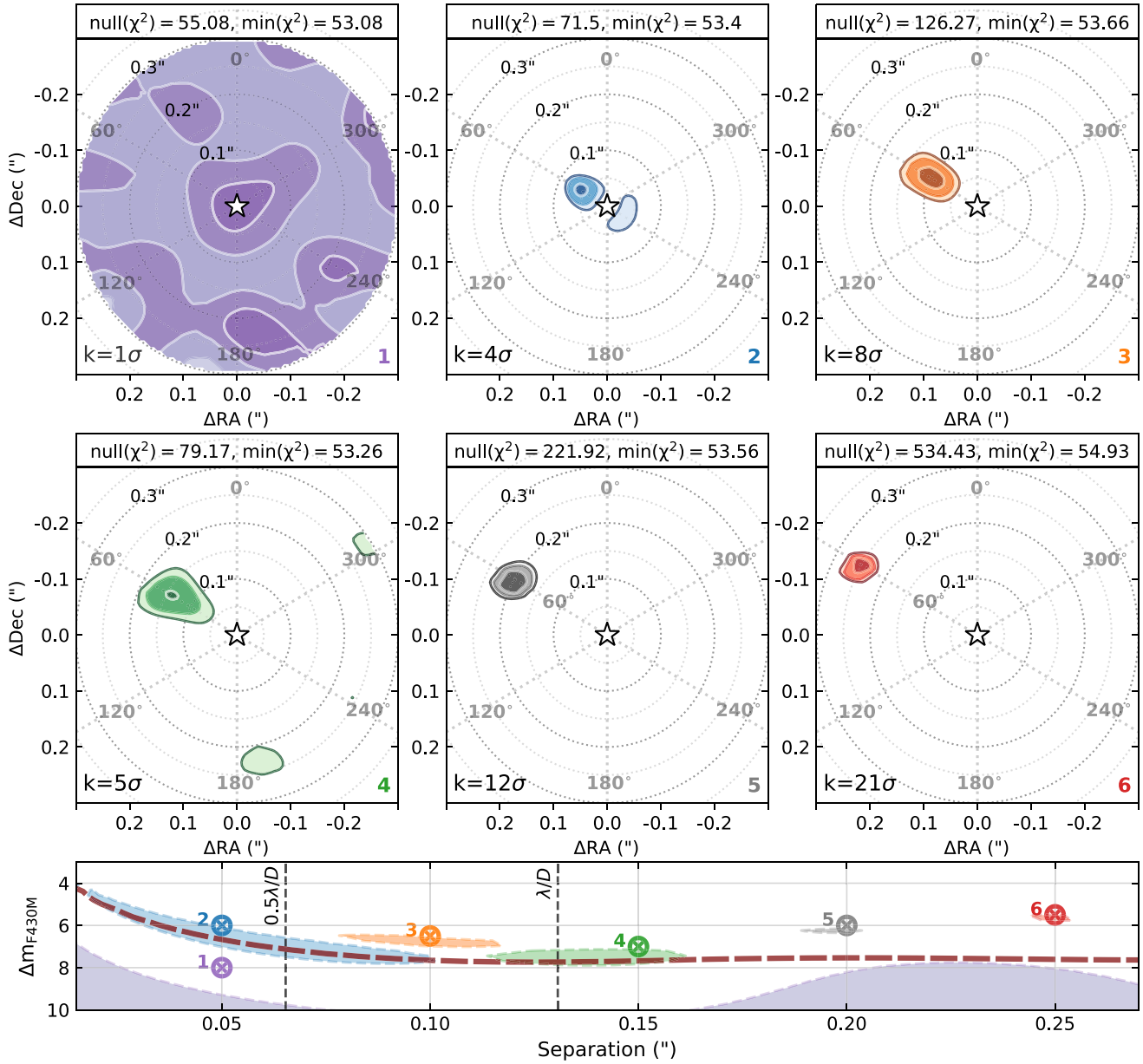

Figure 5. The plots in the first two rows show the χ^2 maps at the best-fit contrast surface slice, with companions injected into the calibrated HIP 65426 data at a fixed position angle ($\theta = 60°$, where θ is calculated counterclockwise with respect to the vertical axis), with varying separations and contrasts for six tests. The null (no-companion) χ^2 values and the minimum χ^2 values are provided at the tops of each of these plots. The test number is provided at the bottom right of each plot. The location of these injections (in the separation vs. contrast space) is shown in the bottom plot, with numbers and color-coded "⊗" symbols. The detection significance (k) of the best fit compared to the null model in each of the plots in the first two rows is given at the bottom left. The grid of concentric circles in the top two panels denotes the separation from the host star (null χ^2 model). For cases with $k > 3\sigma$ (tests 2, 3, 4, 5, and 6), the contour regions are $k\sigma$, $(k-1)\sigma$, and $(k-2)\sigma$ from the null model value, respectively. For test 1, with $k = 1\sigma$, the contours are 1σ, 2σ, and 3σ from the minimum χ^2 value. The bottom panel shows the 1σ region from the best-fit separation and the contrast point for each of the injection tests at the best-fit position-angle slice. The X-axis showing the separation is equivalent to the concentric circles' separation grid in the above plots. The brown dashed line shows the calculated 5σ contrast curve from the HIP 65426 calibrated data (see Figure 6). It is evident that for injections near the contrast limit, companions can be recovered with $\sim 5\sigma$ confidence (even below separations of $0.5\lambda/D$ for test 2, although this causes a larger uncertainty in the retrieved contrast and separation, as seen in the bottom panel). At contrasts brighter than this, the recovered signal significance is considerably larger. However, at separations below $0.5\lambda/D$ and contrasts dimmer than the 5σ limit, the companion cannot be found (test 1 with $k = 1\sigma$ shows a separation/contrast degeneracy in the bottom plot). These results are summarized in Table 4.

(in Figures 3 and 4). Decreasing the companion contrast to levels of $\Delta m_{\mathrm{F380M}} > 7.5$ eventually causes the resulting χ^2 surfaces to become indistinguishable from noise, as in the case of test 1 in Figure 4. For this case, the contour regions are plotted at 1σ, 2σ, and 3σ intervals from the minimum χ^2 value (similar to the plots in Figures 3 and 4). In test 2, a relatively bright companion ($\Delta m_{\mathrm{F380M}} \sim 6.0$) is injected below the Michelson diffraction limit ($0.5\lambda/D$), and hence the recovered signal is not quite as significant ($k = 4\sigma$) as the other cases (with $>0.5\lambda/D$; see Section 4.4 for further discussion). These injection and recovery tests illustrated in Figure 5 are summarized with the relevant values in Table 4. The retrieved values of contrast and separation are the best-fit values obtained from a grid search. And the errors reported on these values in the table are the 1σ errors from the best fit. The corresponding regions are shown in the bottom panel of Figure 5.

Table 4
Summary of the Injection and Recovery Tests Shown in Figure 5 with Their Test Numbers (Increasing in Injected Separation from Test 1 to Test 6)

	Injected Companion		Retrieved Companion					
	$\Delta m_{\mathrm{F380M}}$	Separation (arcsec)	$\Delta m_{\mathrm{F380M}}$	Separation (arcsec)	χ^2_{null}	χ^2_{min}	$\Delta\chi^2$	k-value
1	8.00	0.05	$8.64^{+3.36}_{-1.69}$	$0.23^{+2.77}_{-0.23}$	55.08	53.08	2.00	1σ
2	6.00	0.05	$6.72^{+0.66}_{-2.41}$	$0.06^{+0.03}_{-0.04}$	71.50	53.40	17.10	4σ
3	6.50	0.10	$6.72^{+0.02}_{-0.52}$	$0.10^{+0.02}_{-0.02}$	126.27	53.66	72.61	8σ
4	7.00	0.15	$7.44^{+0.46}_{-0.47}$	$0.14^{+0.02}_{-0.03}$	79.17	53.26	25.91	5σ
5	6.00	0.20	$6.24^{+0.16}_{-0.25}$	$0.20^{+0.00}_{-0.01}$	221.92	53.56	168.36	12σ
6	5.50	0.25	$5.52^{+0.27}_{-0.03}$	$0.25^{+0.00}_{-0.01}$	534.43	54.93	479.50	21σ

Note. The retrieved values are the best-fit values from the grid search. All the retrieved values are listed with 1σ errors from the best fit, rounded off to two decimal places. The k-value is the integer detection significance at the lowest χ^2 value (χ^2_{min}) compared to the null (no-companion) χ^2 value (χ^2_{null}). The injections for all the tests were made at position angle $\theta = 60.^{\circ}00$. The retrieved position angle for all tests was $\theta = 58.^{\circ}78$, with the exception of test 1, which had a retrieved position angle of $\theta = 191.^{\circ}02$.

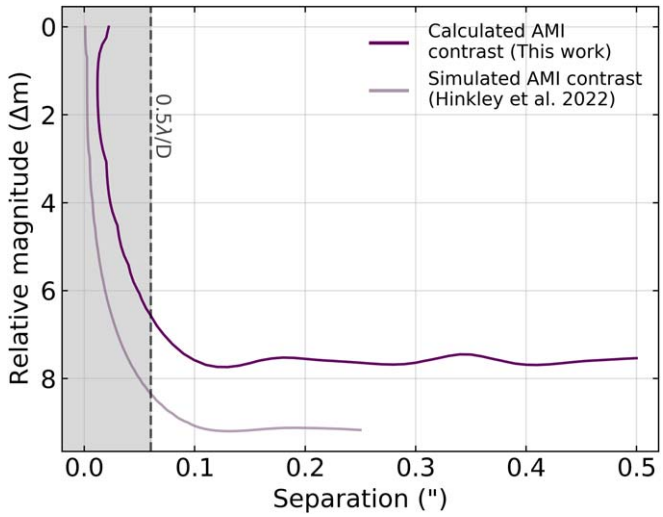

Figure 6. The calculated 5σ contrast curve for our observation is shown in purple, which was obtained using closure phases. The analogous simulated observation is shown in light purple, which was optimistic by ~1–2 mag. The IWA for AMI observations is essentially $0.5\lambda/D$ (the Michelson diffraction limit). Separations below this limit are therefore grayed out. Calculating the mean and the standard deviation of the contrast curve at separations $\geqslant 0.5\lambda/D$ gives a value of $\Delta m = 7.62 \pm 0.13$. This is the contrast we report for this work.

We also show the correlation plots of the injection and recovery tests (with k-values $\geqslant 5\sigma$, as reported in Table 4) with their 1σ errors in the top panel of Figure 7. As is evident from the figure, all these tests (with test numbers 3, 4, 5, and 6) overlap with the 1:1 line within the 1σ error bar, for both separation and contrast values. This establishes that the retrieved values are consistent with the injected values for companions when the signal is detected with $\geqslant 5\sigma$ significance. In the bottom panel of Figure 7, we perform the same injections as in the top panel to a Gaussian distribution. This distribution was produced in the same way as Figure 4, as discussed earlier in this section. In this case, the companion separations and contrasts are also retrieved consistently within the 1σ errors (i.e., they are on the 1:1 dashed gray line, similar to the injection and recovery tests in the calibrated data in the top panel). It is to be noted that the best-fit points in Figure 7 are not on the 1:1 line in any case. This is due to the fact that it is not possible to perfectly recover an injected signal with infinite precision, given that the noise is always going to introduce some error. This is seen in the bottom panel of Figure 7, because the Gaussian distribution does not capture the systematic errors in the actual data, as is the case for all AMI observations (M. J. Ireland 2013). And this is seen in the top panel of Figure 7 as well, with non-Gaussian noise in the data. Although the retrieved values are consistent with the injected signals, the residual systematic errors in the data bias the best-fit values of contrast and separation (which is expected, given the significant non-Gaussian calibration errors). For this reason, we use the null model as a contrast curve estimator. This is further discussed in Section 4.4.

Last, we compare the HIP 65426 data calibrated with HD 116084 to expectations for the signal from the known companion in the system, HIP 65426b (G. Chauvin et al. 2017; A. L. Carter et al. 2023). Figure 8 shows the results. The expected closure-phase signal from HIP 65426b is shown with cyan circles. The calculated closure-phase signal from the observation is shown in maroon with error bars. The smaller error bars are the statistical errors calculated from the science and calibrator observations added in quadrature. The longer error bars are the standard deviations of the calibrated closure phases of the science target (the difference between the science and calibrator observations; see Section 4.2). The spatial frequency of NIRISS/AMI is capable of detecting the aliased signal from the companion. However, Figure 8 shows that the signal from HIP 65426b is at a significantly lower level than the scatter in the calibrated data, making the known companion undetectable.

4.4. Accessible Companion Contrast

A contrast curve was generated from a single-companion fit model. This was executed following an approach similar to S. Sallum et al. (2019), which is briefly discussed here for clarity (see also S. Sallum et al. 2024). The calibrated closure phases and squared visibilities were compared to the closure phases and squared visibilities of a grid of single-companion models with different separations, contrasts, and position angles. For each companion separation, the average χ^2 value of all the sampled position angles (χ^2_{sep}) was calculated. Finally, the 5σ contrast was taken to be the contrast at which $\Delta\chi^2 = \chi^2_{\mathrm{null}} - \chi^2_{\mathrm{sep}} = 25$, where χ^2_{null} is the χ^2 calculated for the null (no-companion; or, equivalently, the position of the

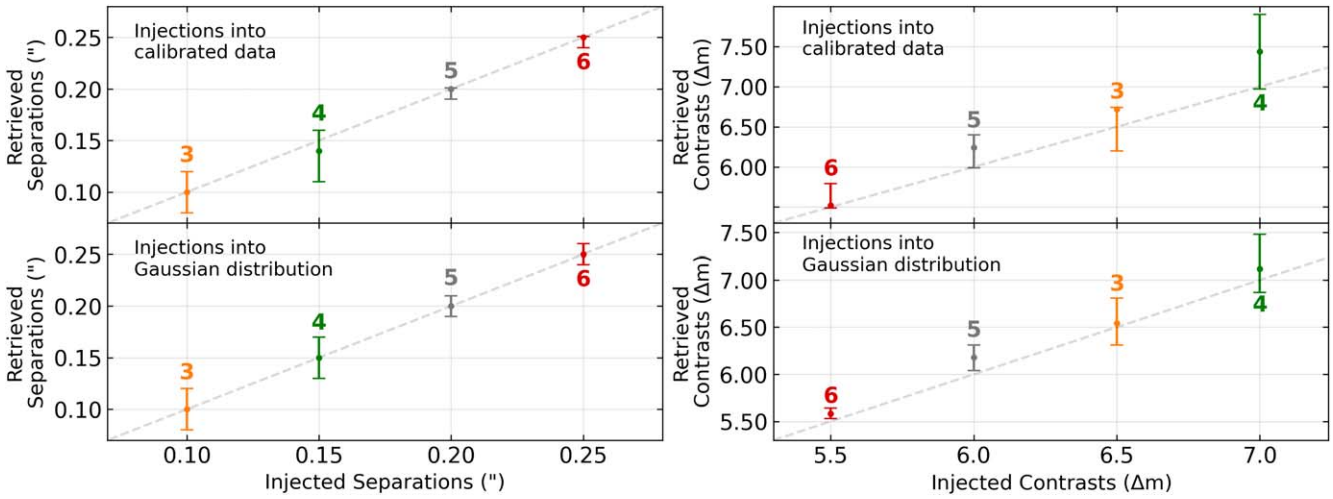

Figure 7. The plots show the correlation between the injected and retrieved values of the companion injections. The left and right panels show the separation and contrast values, respectively. And the top and bottom panels show the injections into calibrated data (the same as in Figure 5) and Gaussian distributions (similar to Figure 4), respectively. The injection tests are at the same contrast and separation values as in Figure 5, with their respective (color-coded) test numbers for tests with k-values $\geqslant 5\sigma$ (see Table 4). The error bars on the plot points are the 1σ errors from the best fit. The retrieved values in the top panel are consistent with the injection values within 1σ (the error bars overlap with the 1:1 straight line, shown in gray), where the injections are into calibrated data. This is also true in the bottom panel, where the injections are into Gaussian distributions of closure phases and squared visibilities, equivalent to the method used to produce Figure 4 and discussed in Section 4.3.

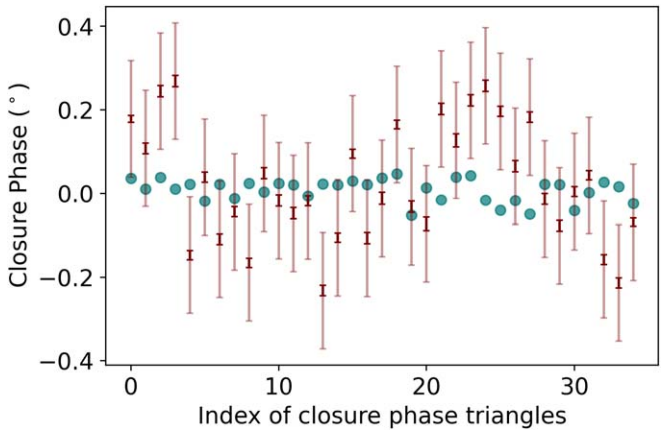

Figure 8. The expected closure-phase signal from the known planet HIP 65426b is shown with cyan circles and the maroon lines are the measured closure phases from the observation. The smaller error bars are the statistical errors (calculated by measuring the scatter around the mean) and the larger error bars are the adopted errors (as discussed in Section 4.2).

star in the χ^2 maps) model. The $\Delta\chi^2$ value of 25 is taken, since one parameter (contrast) determines the difference between the null model and the 5σ detectable model at each separation (refer to S. Sallum et al. 2024 for a detailed description of the contrast curve calculation). This threshold value of $\Delta\chi^2 = 25$ is appropriate for the model selection, as this corresponds to 5σ significance in the case of a model with 1 degree of freedom (the difference in the number of parameters between the companion model and the null model). This 5σ curve is shown in Figure 6 in dark purple. Calculating the mean and the standard deviation of the contrast curve at separations $\geqslant 0\farcs065$ (equivalently $\geqslant 0.5\lambda/D$, the Michelson diffraction limit) gives a value of $\Delta m = 7.62 \pm 0.13$. This is the value we quote for the achievable contrast in this work.

The contrast curve is also shown in Figure 5 in the bottom panel with a dashed brown line. As mentioned briefly in Section 4.3, all injections above this contrast curve (and separations greater than the Michelson diffraction limit of $0.5\lambda/D$) are detected with $\geqslant 5\sigma$ significance. In Figure 5, tests 3, 5, and 6 have high k-values, since all these companions were injected at contrasts brighter than the 5σ contrast limit at the injected separations. Test 4 had a companion injected $\sim$at the 5σ contrast limit and hence is retrieved with 5σ confidence at the injected separation and position angle. There are other regions of low-χ^2 values (for example at separations $\sim 0\farcs2$–$0\farcs3$ with position angles $\sim 190°$ and $\sim 300°$) for this test in the plot (the first plot in the second row of Figure 4) at $\sim 3\sigma$ significance from the null χ^2 value. This is caused by the residual systematic errors in the data.

Test 2 returns a companion with a relatively high confidence ($k = 4\sigma$). However, since this injection is at a separation lower than the Michelson diffraction limit, the grid search struggles to fit the contrast and separation with unique values. This manifests itself in a degeneracy, which can be seen in the bottom panel of Figure 4 (the 1σ region from the best fit at the lowest-χ^2 position-angle slice, shown in blue for test 2). This means that although we can detect the presence of a companion with a contrast greater than the 5σ contrast limit at this separation, we cannot precisely retrieve its orbital location or contrast. For this reason, the corresponding mass limits from this contrast curve were calculated with a lower limit on separation as $0.5\lambda/D$ (see Section 5.2 and Figure 9).

In addition to the calculated 5σ contrast curve, Figure 6 shows the simulated contrast curve of this observation from S. Hinkley et al. (2022) in light purple, based on prelaunch expectations of systematic noise.

5. Discussion

As is evident from Figure 6, the contrast curve from actual data (this work) underperforms compared to the simulated contrast curve of the observation (S. Hinkley et al. 2022). Below, we briefly discuss possible reasons for this discrepancy, which are explored in quantitative detail in the companion Letter (S. Sallum et al. 2024). We also discuss how the

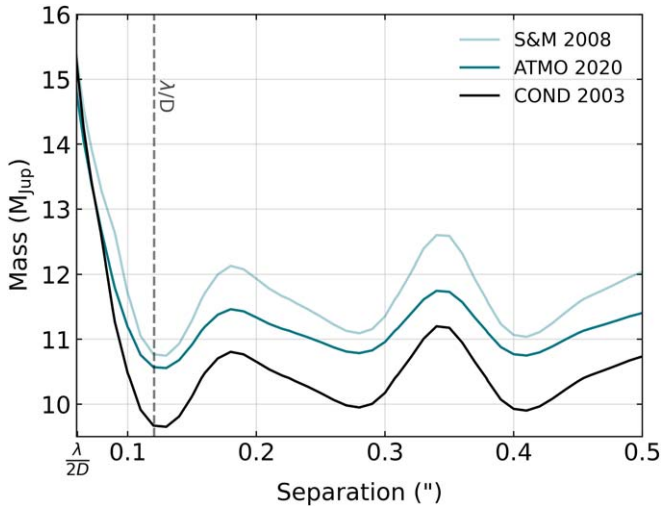

Figure 9. The accessible mass limits using the contrast curve from Figure 6 are shown in this figure. The light cyan curve utilizes the cloudy models from D. Saumon & M. S. Marley (2008), the dark cyan curve utilizes the equilibrium case of ATMO 2020 (M. W. Phillips et al. 2020), and the black curve employs COND 2003 (I. Baraffe et al. 2003). The lower limit on the x-axis is $0.5\lambda/D$, which is approximately the practical achievable IWA with AMI. The dashed gray line shows the conventional diffraction limit below which the contrast curve begins to grow steeply for accessible mass limits.

accessible contrast in magnitudes translates to the accessible mass limits based on different evolutionary models.

5.1. Discrepancy with Simulations

As discussed in detail in S. Sallum et al. (2024), the discrepancy between the simulated and observed contrast curves most likely arises from the fact that the contrast is limited by the effect of charge migration (the *brighter–fatter* effect; e.g., C. M. Hirata & A. Choi 2020), rather than being limited by the photon noise limit. The charge migration effect is exhibited by infrared detectors when the electric field induced by accumulated charges deflects new charges. This causes two nearby pixels to accumulate charge at different rates, with the brighter pixel apparently spilling photoelectrons into its neighboring pixels. For brighter objects, this results in an FWHM of the PSF with larger spatial extent.

In addition to masking the presence of fainter companions in the close vicinity (on the sky plane) of a bright star, charge migration can cause brightness-dependent PSF differences (and thus calibration errors) between a science target and reference PSF target. This effect was not taken into account during the generation of the simulated contrast curve shown in Figure 6. If we had the same level of charge migration between the science and calibrator observations, we would have improved the contrast quality and would have reached closer to the simulated achievable contrast (S. Sallum et al. 2024). To plan observations with this mode in future cycles, observations should ideally target PSF references that are well matched to the science target in brightness.

5.2. Mass Sensitivity Limits

The mass sensitivity accessible with the 5σ calculated contrast curve (see Section 4.4) was calculated using evolutionary models (see Figure 9). An age value of 14 Myr (based on the Lower Centaurus Crux age, which HIP 65426 is a member of, as discussed in Appendix A of G. Chauvin et al. 2017) was used for the analysis across all used models. To account for the uncertainties on the mass limit, different evolutionary models were used that encapsulate different physical processes. These are discussed in the following sections.

5.2.1. ATMO 2020 Atmospheric Models

The mass detection limits were calculated from the generated contrast curve using the ATMO 2020 (M. W. Phillips et al. 2020) set of models, similar to the method in S. Ray et al. (2023). ATMO 2020 is a set of radiative-convective one-dimensional equilibrium cloudless models describing the atmosphere and evolution of cool brown dwarfs and self-luminous giant exoplanets, spanning the mass range of $\sim$0.5–75 $M_{\rm Jup}$. Even though these models are cloudless, they mimic the effect of clouds by using a lower temperature profile. The model is computed in three different sets of evolutionary models: one at chemical equilibrium and two at chemical disequilibrium, assuming vertical mixing at different strengths. We keep our calculations and results limited to the case of the equilibrium models, since this case provides the baseline scenario of planetary atmospheric conditions and does not take into account more complex considerations related to atmospheric dynamics, such as vertical atmospheric mixing (T. S. Barman et al. 2011; Q. M. Konopacky et al. 2013; T. Currie et al. 2023).

It is evident in Figure 9 that, using ATMO 2020, mass values of $\sim$11–12 $M_{\rm Jup}$ are accessible at separations $\sim$0.″1–0.″4 or, equivalently, $\sim$1–3λ/D with our observations using the AMI mode. These separations are smaller than the inner working angles (IWAs) of the JWST coronagraphs ($\sim$0.″36–0.″50). This is achievable due to the combination of the interferometric capability of the AMI mode and the superior infrared sensitivity of JWST.

The accessible mass values coincide with the deuterium-burning mass limit for PMCs (D. S. Spiegel et al. 2011). So the D. Saumon & M. S. Marley (2008) evolutionary models were also explored, which take into account the deuterium burning. This was done using the species toolkit (T. Stolker et al. 2020) and is discussed in the following section.

5.2.2. D. Saumon & M. S. Marley (2008) and COND 2003 Atmospheric Models

The hybrid cloud grid from D. Saumon & M. S. Marley (2008) was used to calculate the mass limits accessible with the given contrast in Figure 6, as this model incorporates deuterium burning. Using this grid of evolutionary models ensures consistency with the ATMO 2020 model (which mimics the effects of clouds) as well as the analysis and calculation of the bolometric flux of HIP 65426b (A. L. Carter et al. 2023), the known companion in the system. Using this model, the mass limits accessible at separations $\sim$0.″1–0.″4 are $\sim$11.0–12.5 $M_{\rm Jup}$ (see Figure 9). This hybrid cloud grid provides a simplified model of the L/T transition by incorporating a cloudy atmosphere at high temperatures ($T_{\rm eff} \geqslant 1400$ K) and a cloud-free atmosphere at low temperatures ($T_{\rm eff} \leqslant 1200$ K). This grid is very similar to COND 2003 (I. Baraffe et al. 2003), and hence the latter was also explored to compute the mass limits in the absence of deuterium burning in the atmosphere of PMCs. Using this model, the mass limits accessible at separations $\sim$0.″1–0.″4 are $\sim$9.5–11.0 $M_{\rm Jup}$ (see Figure 9).

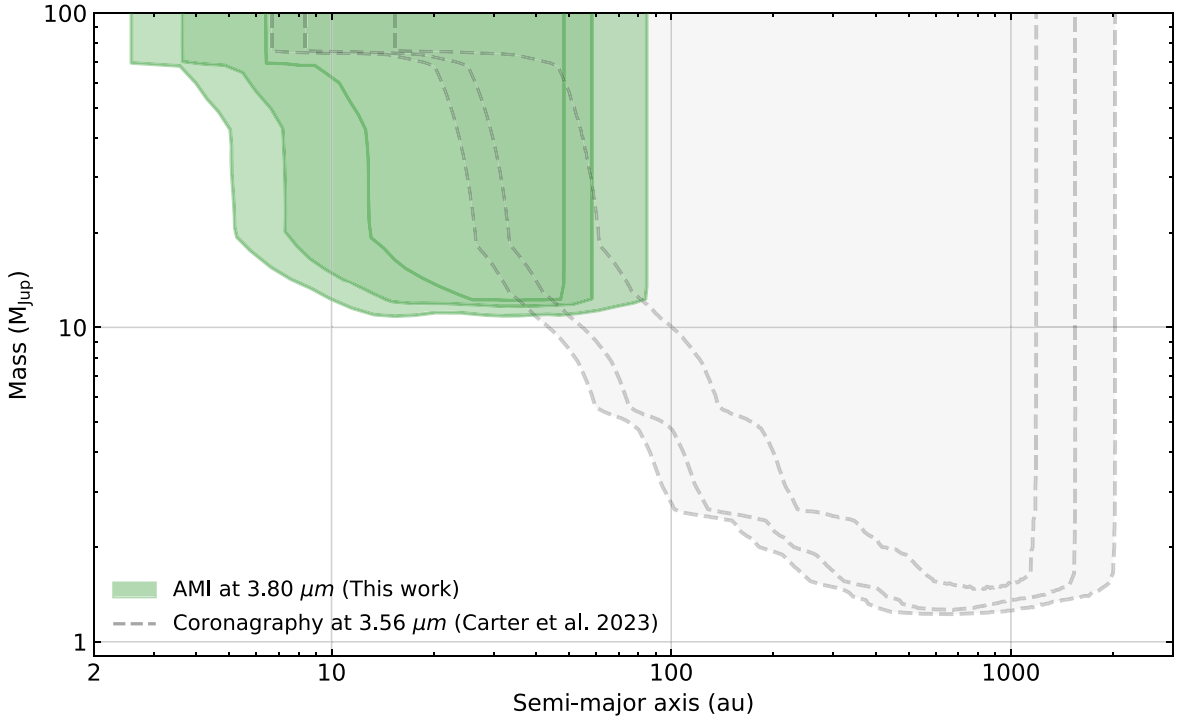

Figure 10. Detection probability maps (contours of 30%, 68%, and 90%) for JWST observations, for the star HIP 65426: the green shows AMI in the F380M filter and the gray dashed lines show coronagraphy in the F356W filter. JWST/AMI reaches close-in separations when compared to coronagraphy at similar wavelengths, probing an essentially unexplored parameter space.

5.3. Mapping the Probability of Detecting Companions

The Exoplanet Detection Map Calculator (`Exo-DMC`; M. Bonavita 2020) was used to estimate a detection probability map using the mass sensitivity limits. This tool uses a Monte Carlo approach to compare the instrument detection limits with a simulated synthetic population of planets with varying orbital geometries around a given star, to estimate the probability of detection of a companion of a given mass and semimajor axis. This information is then summarized in a detection probability map. This PYTHON language tool is an adaptation of the previously existing Multi-purpose Exoplanet Simulation Systemcode (`MESS`) code (M. Bonavita et al. 2012).

Figure 10 shows the detection probability maps for the data set described in this study (AMI at 3.80 μm), as well as one for the coronagraphic observations of the same target obtained at a comparable wavelength (3.56 μm), described in A. L. Carter et al. (2023). The figure clearly shows the exquisite capability of JWST/NIRISS/AMI to detect companions at mid-infrared wavelengths in a completely new orbital parameter space. This can also be seen in Figure 11, where JWST/NIRISS/AMI probes separations lower than that of the VLT/SPHERE/IRDIS observations at H band (1.6 μm; G. Chauvin et al. 2017) for the same object.

In this study, we detect no additional companions, but Figure 10 clearly exhibits the capability of the AMI mode for the investigation of an unexplored parameter space of stellar systems with previously known companions. Figure 4 of G. Chauvin et al. (2017) shows that for this planetary system, regions $\lesssim$20 au are inaccessible by VLT/SPHERE. In Figure 10, we rule out the existence of any additional companions $\gtrsim 10\,M_{\rm Jup}$ at separations $\sim$10–20 au around the host star. These observations hence provide sensitivity inside the classical IWAs of JWST's conventional coronagraphs.

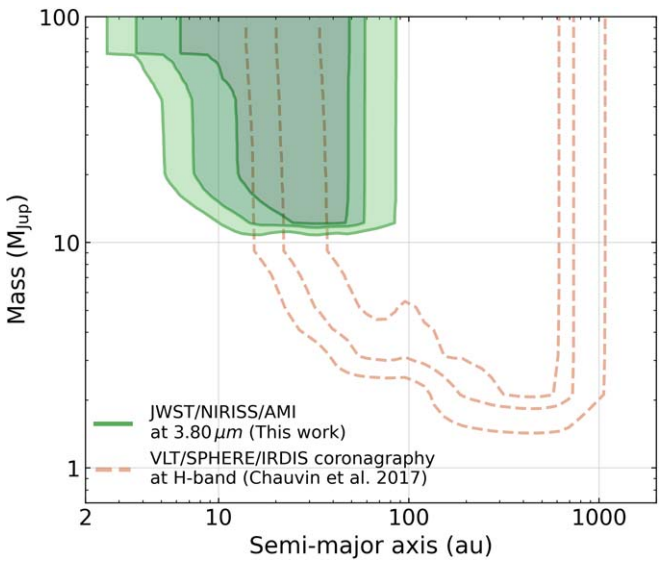

Figure 11. Detection probability maps (contours of 30%, 68%, and 90%) for the AMI observation in the F380M filter with JWST/NIRISS, compared with the coronagraphic H-band observations obtained with VLT/SPHERE/IRDIS (G. Chauvin et al. 2017), for the star HIP 65426.

6. Conclusions

In this study, we have demonstrated that the AMI mode with JWST/NIRISS accesses a completely new parameter space (separations of $\sim$0.″05–0.″5), a region that is only accessible at lower contrast from the ground and is largely inaccessible using the conventional coronagraphs on JWST. This is evident from Figures 10 and 11, which exhibit that with JWST/NIRISS/AMI, companions at solar system planetary scales (as close in as $\sim$10 au) can be accessed. Solely in terms of contrast, the

AMI mode on JWST, with a currently accessible 5σ companion contrast of $\Delta m \sim 7.5$, is still reaching roughly 1 magnitude deeper than very good ground-based AMI performance (e.g., $\Delta m \sim 6.5$ in C. L. Vides et al. 2023, calculated with a similar method). This makes JWST/AMI (even with the underperformance induced by charge migration) the most powerful single-telescope interferometer. And, with more robust reduction techniques and improved observation strategies, this performance will potentially improve in the future.

Going forward, this mode will be the prime technique for detecting companions around stars in the closest star-forming regions at close-in separations. The number of stars in young moving groups available for planet searches is limited to ~100 targets (for example, in the moving groups of β Pictoris and TW Hydrae; S. Ray et al. 2023). However, targeting stars in the Taurus–Auriga or Scorpius–Centaurus associations (which HIP 65426 is a member of) increases the number of such available targets by ~1–2 orders of magnitude, since these associations are potentially rich in thousands of such targets. Opening up the possibility of probing the members of these star formation regions would mean that many promising targets (e.g., those with debris disks, evidence for accretion, or protoplanets using ALMA gas kinematics, etc.) can be probed. These targets could be part of future JWST (and Extremely Large Telescope) observations.

This mode can also be used to find planets in systems that have previously known companions. The characterization of the multiplicity of PMCs around nearby stars would be incomplete without probing inner regions, which JWST/NIRISS/AMI can access. Previous studies (C. Marois et al. 2010; K. Wagner et al. 2019; M. Nowak et al. 2020; S. Hinkley et al. 2023) have shown that additional companions at close-in separations can be found in systems that already have a known companion. This is beyond the capabilities of conventional coronagraphs on JWST, due to their relatively poor IWAs. Hence, observations in future cycles using JWST/NIRISS/AMI will shed some light on this unexplored piece of parameter space.

The angular parameter space (~100–300 mas; see Figure 6) accessible with JWST/AMI for the case of members in nearby stellar associations overlaps the peak sensitivity of current and future ground-based interferometers, such as GRAVITY (S. Lacour et al. 2019; M. Nowak et al. 2020) and BiFROST (S. Kraus et al. 2022). These interferometers can measure dynamical masses of PMCs with high precision (up to ~10%) over a short portion of their orbit (e.g., S. Hinkley et al. 2023). The combination of measurements of precise dynamical masses and the PMC brightness at ~3–5 μm (near the peaks of their spectral energy distributions, or SEDs, giving tightly constrained measurements of bolometric luminosity) is exceedingly powerful for constraining atmospheric and evolutionary models that are highly uncertain at young ages (see Figure 11 of S. Ray et al. 2023). In addition to this, the obtained contrast limits (in Figures 6 and 9) will also access the expected luminosities of circumplanetary disks, whose SEDs can be used to inform planet formation timescales and exomoon formation. Through these applications and more, NIRISS AMI observations in future cycles will provide new, direct constraints on planet formation and evolution.

Acknowledgments

This work is based on observations made with the NASA/ESA/CSA JWST and obtained from the Mikulski Archive for Space Telescopes at the Space Telescope Science Institute. The specific observations analyzed can be accessed via 10.17909/8by2-x206. We are truly grateful for the countless hours that thousands of people have devoted to the design, construction, and commissioning of JWST. We thank the anonymous referee for comments that have been crucial toward the improvement of this Letter. This project was supported by a grant from STScI (JWST-ERS-01386) under NASA contract NAS5-03127. S.R. was supported by the Global Excellence Award at the University of Exeter. This work is based in part on observations obtained at the Southern Astrophysical Research (SOAR) telescope, which is a joint project of the Ministério da Ciência, Tecnologia e Inovações (MCTI/LNA) of Brasil, the US National Science Foundation's NOIRLab, the University of North Carolina at Chapel Hill (UNC), and Michigan State University (MSU). This work has also made use of the SPHERE Data Centre, jointly operated by OSUG/IPAG (Grenoble), PYTHEAS/LAM/CeSAM (Marseille), OCA/Lagrange (Nice), Observatoire de Paris/LESIA (Paris), and Observatoire de Lyon/CRAL, as well as being supported by a grant from Labex OSUG@2020 (Investissements d'avenir—ANR10 LABX56). This work has benefited from the 2022 Exoplanet Summer Program in the Other Worlds Laboratory (OWL) at the University of California, Santa Cruz, a program funded by the Heising–Simons Foundation.

Appendix A
NISRAPID Readout Pattern

Groups and integrations in the "NISRAPID" mode is shown in FIgure 12. This was the mode used by all the observations in this work.

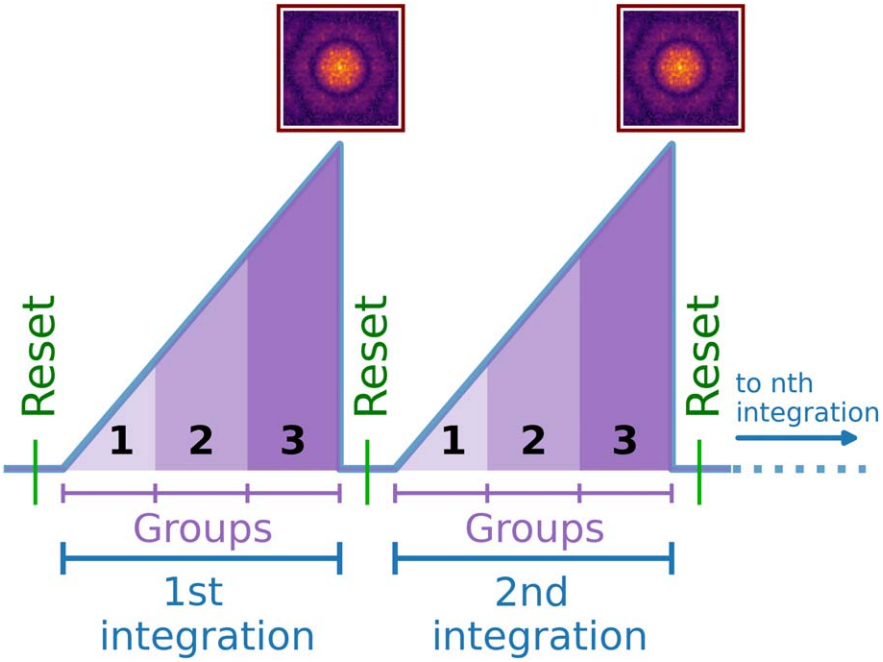

Figure 12. Each purple segment represents a "frame," which is the same as a "group" in this mode and is the smallest unit of exposure. An "integration" is comprised of a number of groups (three, in this case) and represents the total number of photons collected in a contiguous sequence. After each integration, the detector resets and executes the next integration, to collect photons. The total exposure of an observation is the collection of "*n*" such integrations.

Appendix B
Closure Phases of Injected Companion Signals

The calibrated closure phases and the corresponding best fits for the injected companion signals (as discussed in Section 4.3 and Figure 5) are shown in Figure 13.

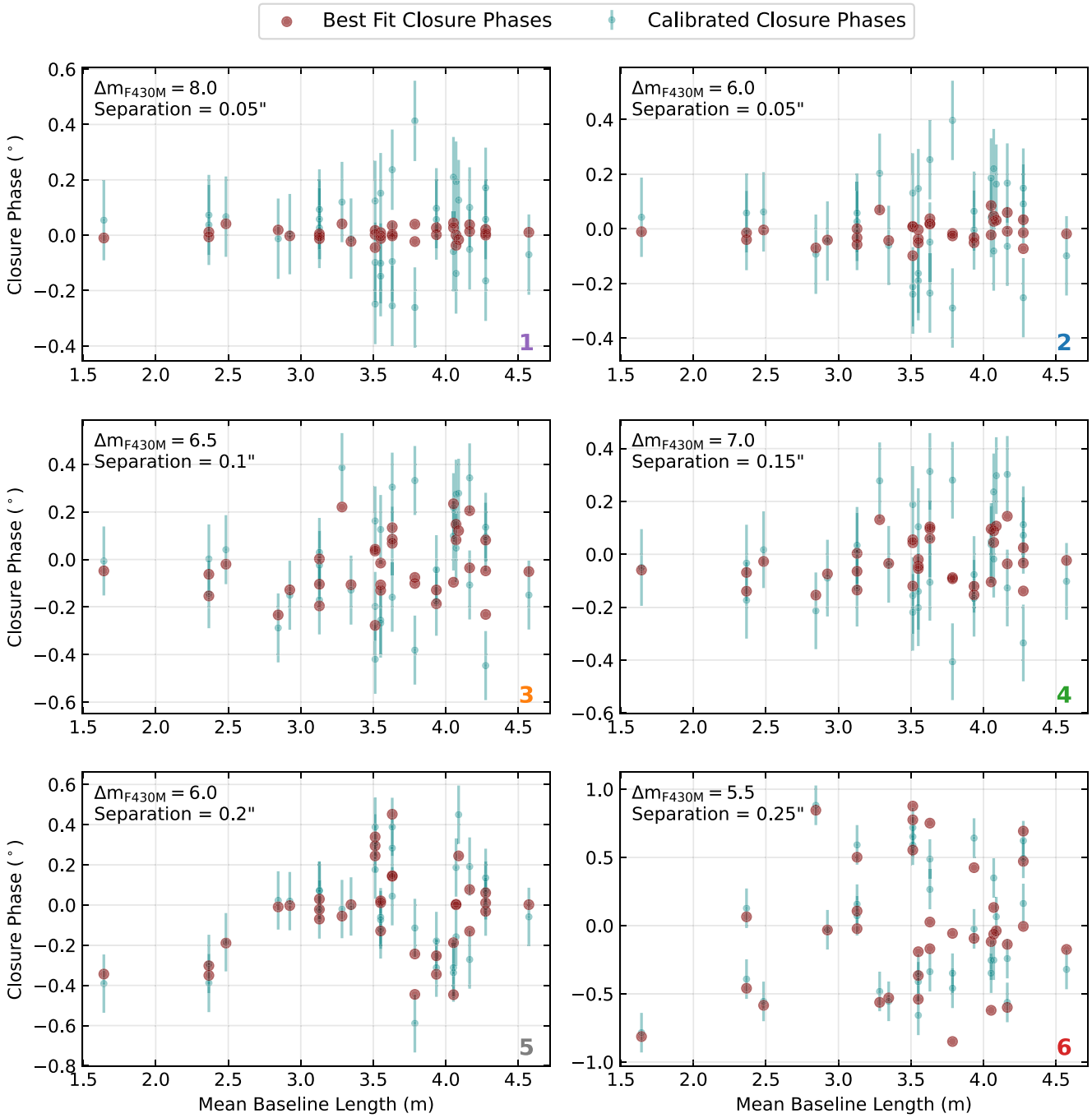

Figure 13. The calibrated closure phases and the corresponding best fits for the injected companion signals. The test numbers are color-coded according to Figure 5, at the bottom right of each plot. The Δm_{F430M} and separation values for each injection are also provided at the top left for each plot.

Appendix C
Squared Visibilities of Injected Companion Signals

The calibrated squared visibilities and the corresponding best fits for the injected companion signals (as discussed in Section 4.3 and Figure 5) are shown in Figure 14.

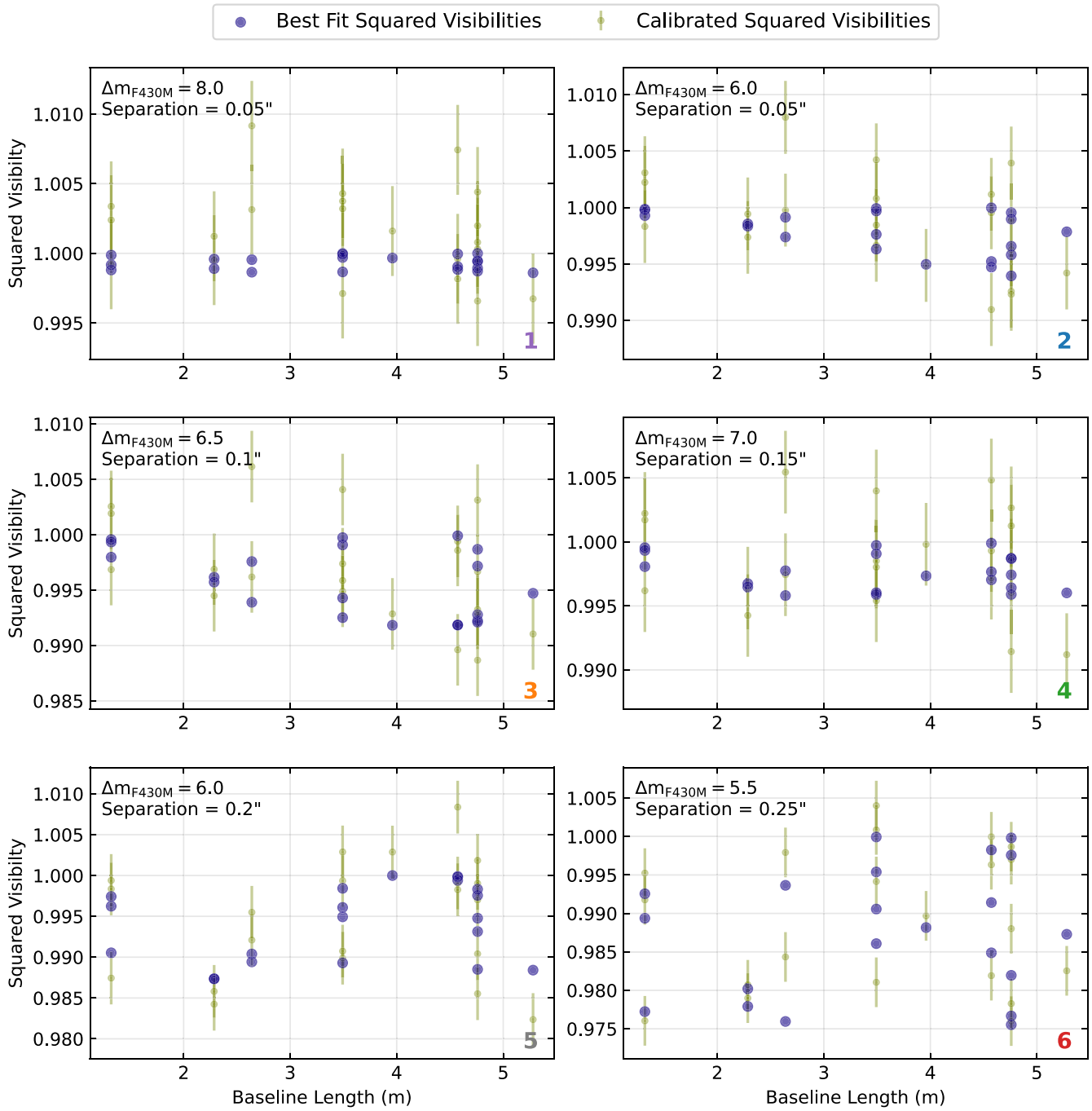

Figure 14. The calibrated squared visibilities and the corresponding best fits for the injected companion signals. The test numbers are color-coded according to Figure 5, at the bottom right of each plot. The $\Delta m_{\mathrm{F430M}}$ and separation values for each injection are also provided at the top left for each plot.

ORCID iDs

Shrishmoy Ray https://orcid.org/0000-0003-2259-3911
Steph Sallum https://orcid.org/0000-0001-6871-6775
Sasha Hinkley https://orcid.org/0000-0001-8074-2562
Jens Kammerer https://orcid.org/0000-0003-2769-0438
Alexandra Z. Greebaum https://orcid.org/0000-0002-7162-8036
Tomas Stolker https://orcid.org/0000-0002-5823-3072
Cecilia Lazzoni https://orcid.org/0000-0001-7819-9003
Andrei Tokovinin https://orcid.org/0000-0002-2084-0782
Samuel Factor https://orcid.org/0000-0002-8332-8516
Jordan M. Stone https://orcid.org/0000-0003-0454-3718
Aarynn Carter https://orcid.org/0000-0001-5365-4815
Beth Biller https://orcid.org/0000-0003-4614-7035
Andrew Skemer https://orcid.org/0000-0001-6098-3924
Genaro Suárez https://orcid.org/0000-0002-2011-4924
Jarron M. Leisenring https://orcid.org/0000-0002-0834-6140
Marshall D. Perrin https://orcid.org/0000-0002-3191-8151
Adam L. Kraus https://orcid.org/0000-0001-9811-568X
Olivier Absil https://orcid.org/0000-0002-4006-6237
William O. Balmer https://orcid.org/0000-0001-6396-8439
Anthony Boccaletti https://orcid.org/0000-0001-9353-2724
Mariangela Bonavita https://orcid.org/0000-0002-7520-8389
Mickael Bonnefoy https://orcid.org/0000-0001-5579-5339
Mark Booth https://orcid.org/0000-0001-8568-6336
Brendan P. Bowler https://orcid.org/0000-0003-2649-2288
Zackery W. Briesemeister https://orcid.org/0000-0002-1764-2494
Marta L. Bryan https://orcid.org/0000-0002-6076-5967
Per Calissendorff https://orcid.org/0000-0002-5335-0616
Faustine Cantalloube https://orcid.org/0000-0002-3968-3780
Gael Chauvin https://orcid.org/0000-0003-4022-8598
Christine H. Chen https://orcid.org/0000-0002-8382-0447
Elodie Choquet https://orcid.org/0000-0002-9173-0740
Valentin Christiaens https://orcid.org/0000-0002-0101-8814
Gabriele Cugno https://orcid.org/0000-0001-7255-3251
Thayne Currie https://orcid.org/0000-0002-7405-3119
Camilla Danielski https://orcid.org/0000-0002-3729-2663
Trent J. Dupuy https://orcid.org/0000-0001-9823-1445
Jacqueline K. Faherty https://orcid.org/0000-0001-6251-0573
Michael P. Fitzgerald https://orcid.org/0000-0002-0176-8973
Jonathan J. Fortney https://orcid.org/0000-0002-9843-4354
Kyle Franson https://orcid.org/0000-0003-4557-414X
Julien H. Girard https://orcid.org/0000-0001-8627-0404
Eileen C. Gonzales https://orcid.org/0000-0003-4636-6676
Thomas Henning https://orcid.org/0000-0002-1493-300X
Dean C. Hines https://orcid.org/0000-0003-4653-6161
Kielan K. W. Hoch https://orcid.org/0000-0002-9803-8255
Callie E. Hood https://orcid.org/0000-0003-1150-7889
Alex R. Howe https://orcid.org/0000-0002-4884-7150
Markus Janson https://orcid.org/0000-0001-8345-593X
Paul Kalas https://orcid.org/0000-0002-6221-5360
Grant M. Kennedy https://orcid.org/0000-0001-6831-7547
Matthew A. Kenworthy https://orcid.org/0000-0002-7064-8270
Pierre Kervella https://orcid.org/0000-0003-0626-1749
Masayuki Kuzuhara https://orcid.org/0000-0002-4677-9182
Kellen Lawson https://orcid.org/0000-0002-6964-8732
Ben W. P. Lew https://orcid.org/0000-0003-1487-6452
Michael C. Liu https://orcid.org/0000-0003-2232-7664
Pengyu Liu https://orcid.org/0000-0001-7047-0874
Jorge Llop-Sayson https://orcid.org/0000-0002-3414-784X
Bruce Macintosh https://orcid.org/0000-0003-1212-7538
Sebastian Marino https://orcid.org/0000-0002-5352-2924
Mark S. Marley https://orcid.org/0000-0002-5251-2943
Christian Marois https://orcid.org/0000-0002-4164-4182
Raquel A. Martinez https://orcid.org/0000-0001-6301-896X
Brenda C. Matthews https://orcid.org/0000-0003-3017-9577
Elisabeth C. Matthews https://orcid.org/0000-0003-0593-1560
Dimitri Mawet https://orcid.org/0000-0002-8895-4735
Johan Mazoyer https://orcid.org/0000-0002-9133-3091
Michael W. McElwain https://orcid.org/0000-0003-0241-8956
Stanimir Metchev https://orcid.org/0000-0003-3050-8203
Michael R. Meyer https://orcid.org/0000-0003-1227-3084
Brittany E. Miles https://orcid.org/0000-0002-5500-4602
Maxwell A. Millar-Blanchaer https://orcid.org/0000-0001-6205-9233
Paul Molliere https://orcid.org/0000-0003-4096-7067
Sarah E. Moran https://orcid.org/0000-0002-6721-3284
Caroline V. Morley https://orcid.org/0000-0002-4404-0456
Sagnick Mukherjee https://orcid.org/0000-0003-1622-1302
Paulina Palma-Bifani https://orcid.org/0000-0002-6217-6867
Eric Pantin https://orcid.org/0000-0001-6472-2844
Polychronis Patapis https://orcid.org/0000-0001-8718-3732
Simon Petrus https://orcid.org/0000-0003-0331-3654
Sascha P. Quanz https://orcid.org/0000-0003-3829-7412
Isabel Rebollido https://orcid.org/0000-0002-4388-6417
Jea Adams Redai https://orcid.org/0000-0002-4489-3168
Bin B. Ren https://orcid.org/0000-0003-1698-9696
Emily Rickman https://orcid.org/0000-0003-4203-9715
Matthias Samland https://orcid.org/0000-0001-9992-4067
Joshua E. Schlieder https://orcid.org/0000-0001-5347-7062
Karl R. Stapelfeldt https://orcid.org/0000-0002-2805-7338
Motohide Tamura https://orcid.org/0000-0002-6510-0681
Xianyu Tan https://orcid.org/0000-0003-2278-6932
Taichi Uyama https://orcid.org/0000-0002-6879-3030
Arthur Vigan https://orcid.org/0000-0002-5902-7828
Malavika Vasist https://orcid.org/0000-0002-4511-3602
Johanna M. Vos https://orcid.org/0000-0003-0489-1528
Kevin Wagner https://orcid.org/0000-0002-4309-6343
Jason J. Wang https://orcid.org/0000-0003-0774-6502
Kimberly Ward-Duong https://orcid.org/0000-0002-4479-8291
Niall Whiteford https://orcid.org/0000-0001-8818-1544
Schuyler G. Wolff https://orcid.org/0000-0002-9977-8255
Kadin Worthen https://orcid.org/0000-0002-5885-5779
Mark C. Wyatt https://orcid.org/0000-0001-9064-5598
Marie Ygouf https://orcid.org/0000-0001-7591-2731
Keming Zhang https://orcid.org/0000-0002-9870-5695
Zhoujian Zhang https://orcid.org/0000-0002-3726-4881
Yifan Zhou https://orcid.org/0000-0003-2969-6040
Alice Zurlo https://orcid.org/0000-0002-5903-8316

B. A. Sargent https://orcid.org/0000-0001-9855-8261
Christopher A. Theissen https://orcid.org/0000-0002-9807-5435
Elena Manjavacas https://orcid.org/0000-0003-0192-6887
Anna Lueber https://orcid.org/0000-0001-6960-0256
Daniel Kitzmann https://orcid.org/0000-0003-4269-3311
Ben J. Sutlieff https://orcid.org/0000-0002-9962-132X
Sarah K. Betti https://orcid.org/0000-0002-8667-6428

References

Baldwin, J. E., Haniff, C. A., Mackay, C. D., & Warner, P. J. 1986, Natur, 320, 595
Baraffe, I., Chabrier, G., Barman, T. S., Allard, F., & Hauschildt, P. H. 2003, A&A, 402, 701
Barman, T. S., Macintosh, B., Konopacky, Q. M., & Marois, C. 2011, ApJ, 733, 65
Bonavita, M., 2020 Exo-DMC: Exoplanet Detection Map Calculator, Astrophysics Source Code Library, ascl:2010.008
Bonavita, M., Chauvin, G., Desidera, S., et al. 2012, A&A, 537, A67
Bonneau, D., Clausse, J. M., Delfosse, X., et al. 2006, A&A, 456, 789
Bushouse, H., Eisenhamer, J., Dencheva, N., et al. 2022, spacetelescope/jwst: JWST v1.6.2, Zenodo, doi: 10.5281/zenodo.6984366
Carter, A. L., Hinkley, S., Kammerer, J., et al. 2023, ApJL, 951, L20
Chauvin, G., Desidera, S., Lagrange, A. M., et al. 2017, A&A, 605, L9
Cheetham, A. C., Girard, J., Lacour, S., et al. 2016, Proc. SPIE, 9907, 99072T
Cheetham, A. C., Samland, M., Brems, S. S., et al. 2019, A&A, 622, A80
Currie, T., Brandt, G. M., Brandt, T. D., et al. 2023, Sci, 380, 198
Doyon, R., Hutchings, J. B., Beaulieu, M., et al. 2012, Proc. SPIE, 8442, 84422R
Doyon, R., Willott, C. J., Hutchings, J. B., et al. 2023, PASP, 135, 098001
Foreman-Mackey, D., Hogg, D. W., Lang, D., & Goodman, J. 2013, PASP, 125, 306
Gardner, J. P., Mather, J. C., Abbott, R., et al. 2023, PASP, 135, 068001
Gardner, J. P., Mather, J. C., Clampin, M., et al. 2006, SSRv, 123, 485
Greenbaum, A. Z., Pueyo, L., Sivaramakrishnan, A., & Lacour, S. 2015, ApJ, 798, 68
Haniff, C. A., Mackay, C. D., Titterington, D. J., Sivia, D., & Baldwin, J. E. 1987, Natur, 328, 694
Hinkley, S., Carter, A. L., Ray, S., et al. 2022, PASP, 134, 095003
Hinkley, S., Kraus, A. L., Ireland, M. J., et al. 2015, ApJL, 806, L9
Hinkley, S., Lacour, S., Marleau, G. D., et al. 2023, A&A, 671, L5
Hirata, C. M., & Choi, A. 2020, PASP, 132, 014501
Ireland, M. J. 2013, MNRAS, 433, 1718
Kammerer, J., Cooper, R. A., Vandal, T., et al. 2023, PASP, 135, 014502
Kammerer, J., Ireland, M. J., Martinache, F., & Girard, J. H. 2019, MNRAS, 486, 639
Konopacky, Q. M., Barman, T. S., Macintosh, B. A., & Marois, C. 2013, Sci, 339, 1398
Kraus, A. L., & Ireland, M. J. 2012, ApJ, 745, 5
Kraus, S., Mortimer, D., Chhabra, S., et al. 2022, Proc. SPIE, 12183, 121831S
Lacour, S., Dembet, R., Abuter, R., et al. 2019, A&A, 624, A99
Lau, R. M., Hankins, M. J., Sanchez-Bermudez, J., et al. 2024, ApJ, 963, 127
Marois, C., Zuckerman, B., Konopacky, Q. M., Macintosh, B., & Barman, T. 2010, Natur, 468, 1080
Miles, B. E., Biller, B. A., Patapis, P., et al. 2023, ApJL, 946, L6
Monnier, J. D., Tuthill, P. G., Danchi, W. C., Murphy, N., & Harries, T. J. 2007, ApJ, 655, 1033
Nowak, M., Lacour, S., Lagrange, A. M., et al. 2020, A&A, 642, L2
Phillips, M. W., Tremblin, P., Baraffe, I., et al. 2020, A&A, 637, A38
Ray, S., Hinkley, S., Sallum, S., et al. 2023, MNRAS, 519, 2718
Readhead, A. C. S., Nakajima, T. S., Pearson, T. J., et al. 1988, AJ, 95, 1278
Rigby, J., Perrin, M., McElwain, M., et al. 2023, PASP, 135, 048001
Sallum, S., Bailey, V., Bernstein, R. A., et al. 2019, BAAS, 51, 527
Sallum, S., Ray, S., & Hinkley, S. 2022, Proc. SPIE, 12183, 121832M
Sallum, S., Ray, S., Kammerer, J., et al. 2024, ApJL, 963, L2
Saumon, D., & Marley, M. S. 2008, ApJ, 689, 1327
Sivaramakrishnan, A., Lafrenière, D., Ford, K. E. S., et al. 2012, Proc. SPIE, 8442, 84422S
Sivaramakrishnan, A., Tuthill, P. G., Ireland, M. J., et al. 2009, Proc. SPIE, 7440, 74400Y
Sivaramakrishnan, A., Tuthill, P., Lloyd, J. P., et al. 2023, PASP, 135, 015003
Soulain, A., Sivaramakrishnan, A., Tuthill, P., et al. 2020, Proc. SPIE, 11446, 1144611
Spiegel, D. S., & Burrows, A. 2012, ApJ, 745, 174
Spiegel, D. S., Burrows, A., & Milsom, J. A. 2011, ApJ, 727, 57
Stolker, T., Quanz, S. P., Todorov, K. O., et al. 2020, A&A, 635, A182
Tokovinin, A., Cantarutti, R., Tighe, R., et al. 2010, PASP, 122, 1483
Tuthill, P. G., Monnier, J. D., & Danchi, W. C. 2001, Natur, 409, 1012
Tuthill, P. G., Monnier, J. D., Danchi, W. C., Wishnow, E. H., & Haniff, C. A. 2000, PASP, 112, 555
Vides, C. L., Sallum, S., Eisner, J., Skemer, A., & Murray-Clay, R. 2023, ApJ, 958, 123
Wagner, K., Apai, D., & Kratter, K. M. 2019, ApJ, 877, 46